Comparison of theoretical and experimental heat diffusivities in the DIII-D edge plasma

W. M. Stacey[a)]
Fusion Research Center, Georgia Tech, Atlanta, Georgia 30332, USA

(Received 26 February 2008; accepted 16 April 2008; published online 30 May 2008)

Predictions of theoretical models for ion and electron heat diffusivity have been compared against experimentally inferred values of the heat diffusivity profile in the edge plasma of two H-modes and one L-mode discharge in DIII-D [J. Luxon, Nucl. Fusion **42**, 614 (2002)]. Various widely used theoretical models based on neoclassical, ion temperature gradient modes, drift Alfvén modes and radiative thermal instability modes for ion transport, and based on paleoclassical, electron temperature gradient modes, trapped electron modes, and drift resistive ballooning modes for electron transport were investigated. © *2008 American Institute of Physics*.
[DOI: 10.1063/1.2920766]

I. INTRODUCTION

The structure of the density and temperature profiles in the edge of tokamak plasmas has long been an area of intense research, at least in part because of the apparent correlation of this structure to global plasma performance. Essential to an understanding of the structure in the edge density and temperature profiles, in the absence or in between edge-localized-modes (ELMs), is an understanding of the underlying transport mechanisms.

A methodology for inferring the underlying heat diffusivities from measurements of temperature and density profiles in the plasma edge, which takes into account convection, atomic physics, and radiation cooling, ion-electron energy exchange and other edge phenomena, has recently been developed and applied to several different types of DIII-D[1] discharges.[2–5] While some comparisons with theoretical formulas have been included in this previous work, the emphasis was on the development of accurate fits of the measured data for use in the inference of experimental heat diffusivity profiles and the accurate calculation of heat and particle fluxes to be used in these inferences. The purpose of this paper is to report a comparison of several theoretical predictions of heat diffusivities with the experimentally inferred heat diffusivities, primarily to gain insight as to the more likely transport mechanisms in the plasma edge, and secondarily to compare some currently used transport models with experiment. To this end, a number of computationally tractable theoretical heat diffusivity models which are widely used for transport modeling have been evaluated using the same experimental data from which the experimental heat diffusivities were inferred.

We note the significant ongoing effort to model transport processes with large-scale gyrokinetic or gyrofluid computer simulations of turbulent transport (e.g., Ref. 6). Such calculations will in the future be able to provide a rigorous test of turbulent transport mechanisms against experiment. However, such calculations for the plasma edge (including the various atomic physics, radiation, and other edge phenomena) are not yet widely available. Thus, we were motivated to undertake a comparison of experimentally inferred heat diffusivities in the edge of DIII-D with the predictions of computationally tractable theoretical models evaluated also using the experimental data, with the intent of obtaining qualitative and semiquantitative physical insights that can provide guidance for future work. Even so, some of the models that we use are state-of-the-art for the particular transport mechanism (e.g., the neoclassical and paleoclassical formulas) and all of them are representative of forms used today by transport modelers to represent heat diffusivities in transport simulations.

The various theoretical models for heat diffusivities are set forth in Sec. II, and the procedure used to infer experimental profiles of heat diffusivity in the edge plasma is briefly summarized in Sec. III. The DIII-D shots used for the comparison are discussed in Sec. IV, where the various experimental data important to the comparison are given. The comparison of the predictions of the theoretical models with the experimentally inferred heat diffusivity profiles is summarized in Sec. V, and the details of the comparison are presented in the Appendix. Finally, the work is summarized in Sec. VI.

II. THEORETICAL THERMAL ENERGY TRANSPORT MODELS

A. Ion transport

1. Neoclassical

The neoclassical Chang–Hinton (neo_ch) expression for the ion thermal conductivity is[7,8]

$$\chi_i^{\text{neoch}} = \varepsilon^{1/2}\rho_{i\theta}^2\nu_{ii}[a_1 g_1 + a_2(g_1 - g_2\ ]), \tag{1}$$

where the a account for impurity, collisional, and finite inverse aspect ratio effects, and the g account for the effect of the Shafranov shift

a)Electronic mail: weston.stacey@nre.gatech.edu.

$$a_1 = \frac{0.66(1+1.54\alpha)+(1.88\sqrt{\varepsilon}-1.54\varepsilon)(1+3.75\alpha)}{1+1.03\sqrt{\mu_j^*}+0.31\mu_j^*},$$

$$a_2 = \frac{0.59\mu_j^*\varepsilon}{1+0.74\mu_j^*\varepsilon^{3/2}}\left[1+\frac{1.33\alpha(1+0.60\alpha)}{1+1.79\alpha}\right], \tag{2}$$

$$g_1 = \frac{1+\frac{3}{2}(\varepsilon^2+\varepsilon\Delta')+\frac{3}{8}\varepsilon^3\Delta'}{1+\frac{1}{2}\varepsilon\Delta'},$$

$$g_2 = \frac{\sqrt{1-\varepsilon^2}\left(1+\frac{\varepsilon\Delta'}{2}\right)}{1+\frac{\Delta'}{\varepsilon}(\sqrt{1-\varepsilon^2}-1)},$$

where $\alpha=n_I Z_I^2/n_i Z_i^2$, $\mu_i^*=\nu_{ii}qR/\varepsilon^{3/2}v_{thi}$ and $\Delta'=d\Delta/dr$, where Δ is the Shafranov shift. The impurity thermal conductivity is obtained by interchanging the i and I subscripts in the above expressions.

The Shafranov shift parameter may be evaluated from[9]

$$\Delta' \equiv \frac{d\Delta}{dr} = -\frac{1}{RB_\theta^2}\left(\frac{r^3}{a^2}\beta_\theta B_{\theta a}^2+\frac{1}{r}\int_o^r B_\theta^2 r'dr'\right), \tag{3}$$

where $\beta_\theta=p/(B_\theta^2/2\mu_0)$ and $B_{\theta a}$ denotes the poloidal magnetic field evaluated at $r=a$. Since we need this quantity at $r\approx a$, we can take advantage of the definition of the internal inductance

$$l_i = \frac{2\int_o^a B_\theta^2 r'dr'}{a^2 B_{\theta a}^2}, \tag{4}$$

where $\beta_{\theta a}$ denotes the quantity evaluated using the average pressure over the plasma and $B_{\theta a}$ is the poloidal magnetic field evaluated at the last closed flux surface (LCFS). Using a parabola-to-a-power current profile $j(r)=j_0[1-(r^2/a^2)]^\nu$, for which the ratio of the values of the safety factor at the edge to the center is $q_a/q_0=\nu+1$, and a fit,[9] $l_i=\ln(1.65+0.89\nu)$ leads to the simple expression

$$\Delta' = -\frac{a}{R}\left(\bar{\beta}_{\theta a}+\frac{1}{2}l_i\right) = -\frac{a}{R}\left\{\bar{\beta}_{\theta a}+\frac{1}{2}\ln\left[1.65+0.89\left(\frac{q_a}{q_o}-1\right)\right]\right\}. \tag{5}$$

In the presence of a strong shear in the radial electric field, the particle banana orbits are squeezed, resulting in a reduction in the ion thermal conductivity by a factor of $S_E^{-3/2}$, where[10]

$$S_E = \left|1-\rho_{i\theta}\left(\frac{d\ln E_r}{dr}\right)\left(\frac{E_r}{v_{thi}B_\theta}\right)\right|. \tag{6}$$

Here $\rho_{i\theta}$ is the ion poloidal gyroradius.

The neoclassical transport phenomena are always present and are believed to constitute an irreducible minimum for transport.

2. Ion temperature gradient (ITG) modes

The ITG modes are believed to be among the most likely of several drift wave instabilities which could be responsible for anomalous thermal transport. For a sufficiently large ion temperature gradient $[L_{Ti}\equiv -T_i/(dT_i/dr)<L_{Ti}^{crit}]$ the toroidal ion temperature gradient (ITG) modes become unstable. In the large aspect ratio, low beta limit, the critical temperature gradient for the destabilization of ITG modes can be written[11]

$$\left(\frac{R}{L_{Ti}}\right)_{crit} = \max\left[\begin{array}{l} 0.8R/L_{ne}, \text{ or} \\ (1+1/\tau)\left(1.33+1.91\frac{r}{q^2}\frac{dq}{dr}\right)(1-1.15\varepsilon)\end{array}\right] \tag{7}$$

where $\tau\equiv Z_{eff}T_e/T_i$. For $R/L_{Ti}<(R/L_{Ti})_{crit}$, the toroidal ETG modes are linearly stable, but for $R/L_{Ti}>(R/L_{Ti})_{crit}$ these modes are unstable and produce thermal ion transport.

Several early gyro-Bohm expressions (e.g., Ref. 12) for the heat diffusivity of the ITG modes take the form

$$\chi_i^{ITG} = \frac{5}{4}\left(\frac{1}{RL_{Ti}}\right)^{1/2}\left(\frac{\rho_i T_e}{e_i B}\right)H[R/L_{Ti}-(R/L_{Ti})_{crit}], \tag{8}$$

where H is the Heaviside function, ρ_i is the ion gyroradius in the toroidal magnetic field B, and $k_\perp\rho_i=2$ has been used.

More recently, Horton *et al.*[13,14] combined semiquantitative knowledge of microturbulence with information from experiments to develop an expression for the ion thermal diffusivity due to the ITG modes. They argued that transport over a scale much larger than the radial correlation length λ_c of the turbulence but much less than the minor radius of the plasma must be governed by diffusive processes with a local thermal diffusivity that depends on the local features of the turbulence, i.e., $\chi_i=(\lambda_c^2/\tau_c)f(v_{E\times B}\tau_c/\lambda_c)$, where τ_c is a characteristic time. They then combined the condition for marginal stability of the ITG modes $(T_e/eB)(k_\theta L_{Ti})\approx c_s/qR$ with the fact that the propagation time for ion acoustic waves over the effective parallel distance qR of the system is qR/c_s to estimate the cutoff wavenumber $k_\perp^{cut}\approx\rho_s(qR/L_{Ti})$. (The symbol ρ_s is widely used for the ion gyroradius, and we will use both this symbol and ρ_i.) Assuming that the radial and poloidal correlation lengths are the same, they then estimated the radial correlation length $\lambda_c\approx\rho_s(qR/L_{Ti})$. The maximum value of the growth rate $\gamma\approx v_{thi}(k_\perp\rho_s)/\sqrt{RL_{Ti}}$ occurs for $(k_\perp\rho_s)\approx 1/2$. Estimating the characteristic time as the inverse of the maximum growth rate then yields[13]

$$\chi_i^{ITG} = C_i q^2\left(\frac{T_e}{eB}\right)\left(\frac{\rho_s}{L_{Ti}}\right)\left(\frac{R}{L_{Ti}}\right)^{3/2}, \tag{9a}$$

where C_i was interpreted to be a measure of the fraction to which the turbulence reached the full mixing length level $\ell/L_T\simeq e\phi/T$ and was determined to be $C_i=0.014$ by fitting the above formula to experimental data from Tore Supra.[14] We will use this value of C_i. Equation (9a) predicts a stronger dependence on the ion temperature gradient than does Eq. (8). If instead the characteristic time was estimated as the inverse of the linear growth rate with $k_\perp\approx 1/2\rho_s$ the estimate of the ion thermal diffusivity is instead[13]

$$\chi_i^{\mathrm{ITG}} = C_i q \left(\frac{T_e}{eB}\right)\left(\frac{\rho_s}{L_{Ti}}\right)\left(\frac{R}{L_{Ti}}\right)^{1/2}. \tag{9b}$$

A more complete treatment of the transport due to toroidal ITG modes was developed by Weiland.[15] The model was developed from a linear stability analysis of the continuity, momentum, and energy balance equations, resulting in a dispersion relation that must be calculated numerically. In this paper we will use the wave number at which the maximum transport for ITG modes occurs, $k_\perp = 0.3/\rho_s$, rather than solving the dispersion relation. The resulting ion transport is derived from the quasilinear approximation and can be considered a version of ITG, and the electron transport can be considered a version of TEM (trapped electron mode).

The onset (instability) condition for this toroidal ITG mode is

$$\eta_i > \eta_{ith} = \frac{2}{3} - \frac{\tau}{2} + \varepsilon_n\left(\frac{\tau}{4} + \frac{10}{9\tau}\right) + \frac{\tau}{4\varepsilon_n} - \frac{k_\perp^2\rho_s^2}{2\varepsilon_n}\left[\frac{5}{3} - \frac{\tau}{4} + \frac{\tau}{4\varepsilon_n} - \left(\frac{10}{3} + \frac{\tau}{4} - \frac{10}{9\tau}\right)\varepsilon_n + \left(\frac{5}{3} + \frac{\tau}{4} - \frac{10}{9\tau}\right)\varepsilon_n^2\right], \tag{10}$$

where

$$\eta_{i,e} \equiv \frac{L_n}{L_{Ti,e}}, \quad \tau \equiv \frac{Z_{\mathrm{eff}}T_e}{T_i}, \quad \varepsilon_n \equiv \frac{2L_n}{R}. \tag{11}$$

The quasilinear estimates for the thermal diffusivities in the Weiland model were constructed by estimating the turbulent heat fluxes and then assuming they satisfied a Fick's law (i.e., were conductive). We will distinguish such effective thermal diffusivities which also indirectly account for any convective heat fluxes by referring to them as effective heat diffusivities. The effective ion heat diffusivity obtained in this way is

$$(\chi_i^{\mathrm{ITG}})_{\mathrm{eff}} = \frac{1}{\eta_i}\left[\eta_i - \frac{2}{3} - \frac{10}{9}\frac{\varepsilon_n}{\tau}\right]\frac{\gamma^3/k^2}{\left(\omega_r - \frac{5}{3}\omega_{Di}\right)^2 + \gamma^2} \tag{12a}$$

if parallel ion motion and trapped particle effects are neglected, and is

$$(\chi_i^{\mathrm{ITG}})_{\mathrm{eff}} = \frac{1}{\eta_i}\left[\eta_i - \frac{2}{3} - (1-f_{\mathrm{tr}})\frac{10}{9}\frac{\varepsilon_n}{\tau} - \frac{2}{3}f_{\mathrm{tr}}\Delta_i\right] \times \frac{\gamma^3/k^2}{\left(\omega_r - \frac{5}{3}\omega_{Di}\right)^2 + \gamma^2}, \tag{12b}$$

when they are taken into account. The drift frequencies are calculated from the curvature and grad-B drifts

$$\omega_{Di} = \frac{3kT_i}{eB_\phi R}, \quad \omega_{De} = -\frac{3kT_e}{eB_\phi R} \tag{13}$$

and from the density gradients

$$\omega_{*i} = -\frac{kT_i}{eB_\phi L_n}, \quad \omega_{*e} = \frac{kT_e}{eB_\phi L_n} \tag{14}$$

the growth rate of the mode is

$$\gamma = \frac{\omega_{*e}\sqrt{\varepsilon_n/\tau}}{1 + k^2\rho_s^2}\sqrt{\eta_i - \eta_{ith}} \tag{15}$$

the oscillatory frequency of the mode is

$$\omega_r = \frac{1}{2}\omega_{*e}\left[1 - \varepsilon_n\left(1 + \frac{10}{3\tau}\right) - k^2\rho_s^2\left(1 + \frac{1+\eta_i}{\tau} - \varepsilon_n - \frac{5\varepsilon_n}{3\tau}\right)\right] \tag{16}$$

and the quantity Δ_i is

$$\Delta_i = \frac{1}{N}\left\{|\hat{\omega}|^2\left[|\hat{\omega}|^2(\varepsilon_n - 1) + \hat{\omega}_r\varepsilon_n\left(\frac{14}{3} - 2\eta_e - \frac{10}{3}\varepsilon_n\right) + \frac{5}{3}\varepsilon_n^2\left(-\frac{11}{3} + 2\eta_e + \frac{7}{3}\varepsilon_n\right) - \frac{5}{3\tau}\varepsilon_n^2\left(1 + \eta_e - \frac{5}{3}\varepsilon_n\right)\right] + \frac{50}{9\tau}\hat{\omega}_r\varepsilon_n^3(1-\varepsilon_n) - \frac{25}{9\tau}\left(\frac{7}{3} - \eta_e - \frac{5}{3}\varepsilon_n\right)\right\}, \tag{17}$$

where

$$\hat{\omega}_r = \frac{\omega_r}{\omega_{*e}}, \quad \hat{\gamma} = \frac{\gamma}{\omega_{*e}}, \quad |\hat{\omega}|^2 = \hat{\omega}_r^2 + \hat{\gamma}^2 \tag{18}$$

and

$$N = \left(\hat{\omega}_r^2 - \hat{\gamma}^2 - \frac{10}{3}\hat{\omega}_r\varepsilon_n + \frac{5}{3}\varepsilon_n^2\right)^2 + 4\hat{\gamma}^2\left(\hat{\omega}_r - \frac{5}{3}\varepsilon_n\right)^2. \tag{19}$$

A simplification of the Weiland formalism (in which the form for the particle diffusion coefficient is used also for the ion heat diffusivity) is given by the Kalupin *et al.*[16] estimate

$$(\chi_i^{\mathrm{ITG}})_{\mathrm{eff}} = \frac{\rho_i T_e}{0.3eB_\phi}\left[\left(L_{Ti}^{-1} - \frac{2}{3}L_n^{-1}\right)\frac{1}{\tau R(1-f_{\mathrm{tr}})} - \frac{1}{8}\left(\frac{2}{R} - L_n^{-1}\right)^2(1-f_{\mathrm{tr}})^{-2} - \frac{20}{9}\frac{1}{\tau^2R^2}\right]^{1/2} \tag{20}$$

used in transport simulations by the Julich group,[16] where $k_{\mathrm{ITG}} \simeq 0.3/\rho_i$ has been used to represent the ITG modes causing the largest transport in an improved mixing length approximation.

When $R/L_{Ti} > (R/L_{Ti})_{\mathrm{crit}}$, or $\eta_i > \eta_{ith}$, the ITG modes are unstable and produce transport. However, the transport predicted by Eqs. (8), (9a), (9b), (12a), (12b), and (20) does not take into account the predicted[17] damping of the growth rates of these modes by $E\times B$ shear. The ITG modes are predicted to be substantially suppressed by $E\times B$ flow shear when the $E\times B$ shearing rate for turbulent eddies

$$\omega_{E\times B} \equiv \left|\frac{RB_\theta}{B_\phi}\frac{\partial}{\partial r}\left(\frac{E_r}{RB_\theta}\right)\right| \tag{21}$$

is comparable to or greater than the maximum linear growth rate $\gamma_{\mathrm{max}}^{\mathrm{ITG}}$ of the mode spectrum.[18] For the ITG mode with the greatest transport the wave number is[13] $k \simeq 0.3/\rho_s$, and the maximum growth rate is[13] $\gamma_{\mathrm{max}}^{\mathrm{ITG}} \simeq 0.3c_s/(L_{Ti}R)^{1/2}$ $(c_s = \sqrt{T_e/m_i})$. This $E\times B$ suppression can be represented by the multiplicative shear suppression factor[19,20]

$$F_s^{\mathrm{ITG}} = \frac{1}{1+(Y_s^{\mathrm{ITG}})^2}, \quad Y_s^{\mathrm{ITG}} = \omega_{E\times B}/\gamma_{\max}^{\mathrm{ITG}} \tag{22}$$

so that the transport rates of Eqs. (8), (9a), (9b), (12a), (12b), and (20) are reduced to

$$\hat{\chi}_i^{\mathrm{ITG}} = F_s^{\mathrm{ITG}}(\omega_{E\times B})\chi_i^{\mathrm{ITG}} \tag{23}$$

by $E\times B$ flow shear.

An additional magnetic shear $[S_m \equiv (r/q)(dq/dr)]$ suppression factor $G(S_m)$ has been introduced empirically into transport simulations to obtain better agreement with experiment.[19–22] Such magnetic shear stabilization could be related to the dependence of the ITG thermal diffusivity on magnetic field[23] and/or to the predicted[24] reduction in the heat diffusivity of high radial ITG modes with increasing magnetic shear. Thus, the $E\times B$ flow and magnetic shear-suppressed ion thermal diffusivity due to ITG modes can be represented as[19]

$$\tilde{\chi}_i^{\mathrm{ITG}} = G(S_m)\hat{\chi}_i^{\mathrm{ITG}} = G(S_m)F_s^{\mathrm{ITG}}(\omega_{E\times B})\chi_i^{\mathrm{ITG}}. \tag{24}$$

In this work, we follow Ref. 21 in using $G(S_m)=S_m^{-1.8}$ to represent the additional magnetic shear-suppression.

3. Drift Alfvén modes

Drift Alfvén (da) instabilities are driven by collisions and hence become important in the more collisional edge plasma. Numerical modeling[25] indicates that $E\times B$ shear alone cannot stabilize these modes (low collisionality and a steep pressure gradient are also needed). An analytical model[26] which takes these effects into account yields the expression

$$\chi_i^{\mathrm{da}} = \chi_i^{\mathrm{gb}}\bar{\bar{\chi}}_\perp(\beta_\parallel, \nu_n)/\sqrt{\mu}, \tag{25}$$

where the ion gyro-Bohm thermal conductivity is $\chi_i^{\mathrm{gb}}=\rho_s^2 c_s/L_{pi}$, with $L_{pi}\equiv -p_i/(dp_i/dr)$,

$$\mu = -k_\parallel L_{pi}\sqrt{m_i T_e/m_e T_i} \simeq -\frac{L_{pi}}{qR}\sqrt{m_i T_e/m_e T_i} \tag{26}$$

for $k_\parallel \simeq 1/qR$, and

$$\bar{\bar{\chi}}_\perp = \left[\frac{(1+\beta_n^2)^{-3}+\nu_n^2}{1+\beta_n^2+\nu_n^{4/3}}\right]^{1/2}, \tag{27}$$

where

$$\beta_n \equiv \left(\frac{m_i}{m_e}\right)^{1/2}\beta\frac{qR}{L_{pi}}, \quad \beta = \frac{n_e T_e}{B^2/2\mu_0},$$
$$\nu_n \equiv \left(\frac{m_i}{m_e}\right)^{1/4}\frac{(qRL_{pi})^{1/2}}{\lambda_e} \tag{28}$$

with $\lambda_e = v_{\mathrm{the}}/\nu_{ei}$ being the electron mean free path.

4. Thermal instabilities

In the weak ion-electron equilibration limit, local radial thermal instabilities in the edge ion and electron energy balances are decoupled, and the linear growth rates may be written in the general form[27]

$$\gamma = -\frac{2}{3}\left[\chi_0(\nu L_T^{-2}+k_r^2)+\frac{5}{2}\nu\frac{\Gamma_\perp}{n}L_T^{-1}-\alpha\right], \tag{29}$$

where the first two terms represent the generally stabilizing effect of heat conduction and convection, respectively, with $L_T^{-1}=(-dT/dr)/T$ for the species in question, $\Gamma_\perp$ being the ion or electron particle flux, and ν characterizing the temperature dependence of the underlying thermal conductivity for that species, $\chi_0 \sim T^\nu$. We use $\nu=2.5$, but the results are relatively insensitive to this value. (There is a similar result in the strong equilibration limit.[27]) The α-terms represent the generally destabilizing atomic physics and impurity cooling terms in the respective growth rates for the ions

$$\alpha_i = \frac{5}{2}(\nu-1)\nu_{\mathrm{ion}} + \frac{3}{2}\nu_{\mathrm{at}}^c\left[\nu - \left(1+\frac{T_i}{\nu_{\mathrm{at}}^c}\frac{\partial\nu_{\mathrm{at}}^c}{\partial T_i}\right)\right] - \frac{1}{n}\left(\nu\frac{H_i}{T_i}-\frac{\partial H_i}{\partial T}\right) \tag{30a}$$

and for the electrons

$$\alpha_e = n_z\left(\frac{\nu L_z}{T_e}-\frac{\partial L_z}{\partial T_e}\right) + \nu_{\mathrm{ion}}\left[\frac{5}{2}(\nu-1)+\nu\frac{E_{\mathrm{ion}}}{T_e} - \left(\frac{3}{2}+\frac{E_{\mathrm{ion}}}{T_e}\right)\frac{T_e}{\nu_{\mathrm{ion}}}\frac{\partial\nu_{\mathrm{ion}}}{\partial T_e}\right] - \frac{1}{n}\left(\nu\frac{H_e}{T_e}-\frac{\partial H_e}{\partial T_e}\right). \tag{30b}$$

The terms ν_{ion} and ν_{at} are the neutral ionization frequency in the pedestal region and the frequency of charge-exchange plus elastic scattering events involving "cold" neutrals that have not previously undergone such an event in the pedestal region. E_{ion} is the ionization energy, and n_z and L_z are the density and radiative emissivity of impurities in the edge pedestal region. H represents any additional heating or cooling in the pedestal.

A mixing length estimate of the transport associated with such thermal instabilities (ti) is

$$\chi_{i,e}^{\mathrm{ti}} \simeq \gamma_{i,e}k_r^{-2}. \tag{31}$$

In the numerical evaluation, we use the neoclassical and paleoclassical values of the ion and electron thermal diffusivities to evaluate the "background" χ_0 in Eq. (29). When the calculated growth rate is negative, the thermal instabilities are not present.

B. Electron transport

1. Paleoclassical

Callen's model[28] based on classical electron heat conduction along field lines and magnetic field diffusion in which the electron temperature equilibrates within a distance L along the field lines and in which radially diffusing field lines carry this equilibrated temperature with them and thus induce a radial electron heat transport $M \simeq L/\pi qR \sim 10$ times larger than the resistive magnetic field diffusion rate leads to the following paleoclassical (paleo) expression for the electron heat diffusivity:

$$\chi_e^{\text{paleo}} = 1.5(1+M)\frac{\eta_\parallel^{nc}}{\eta_0}\nu_e\delta_e^2. \tag{32}$$

Taking L as the minimum of the electron collision mean free path or the maximum half length of the helical field results in

$$M = \frac{1/\pi Rq}{1/\ell_{\max} + 1/\lambda_e}, \tag{33}$$

where

$$\delta_e^2\nu_e = \frac{1.4x10^3 Z_{\text{eff}}}{T_e^{3/2}(eV)}\left(\frac{\ln\Lambda}{17}\right), \quad \delta_e = c/\omega_{pe},$$

$$\ell_{\max} \equiv \frac{\pi Rq_*}{\left(\pi\bar{\delta}_e\frac{dq}{d\rho}\right)^{1/2}} = \frac{R\sqrt{\pi q}}{\left[\frac{\delta_e}{a}\left(\frac{1}{q}\frac{dq}{d\rho}\right)\right]^{1/2}},$$

$$\frac{\eta_\parallel^{nc}}{\eta_0} = \left(\frac{\sqrt{2}+Z_{\text{eff}}}{\sqrt{2}+13Z_{\text{eff}}/4}\right) + \left[\frac{\sqrt{2}+Z_{\text{eff}}-\ln(1+\sqrt{2})}{Z_{\text{eff}}(1+\nu_{*e}^{1/2}+\nu_{*e})}\right]\frac{(1-f_c)}{f_c}, \tag{34}$$

$$f_c \simeq \frac{(1-\varepsilon^2)^{-1/2}(1-\varepsilon)^2}{1+1.46\varepsilon^{1/2}+0.2\varepsilon},$$

$$\nu_{*e} = Rq/\varepsilon^{3/2}\lambda_e, \quad \lambda_e = \frac{1.2x10^{16}T_e^2(eV)}{n_e Z_{\text{eff}}}\left(\frac{17}{\ln\Lambda}\right).$$

The quantity f_c is the fraction of circulating particles, and $f_{\text{tr}}=1-f_c$ is the trapped fraction. The paleoclassical transport phenomena are always present and are believed to constitute an irreducible minimum level of electron transport.[28]

The paleoclassical heat transport is not in the conventional form $q_e=-n_e\chi_e\nabla T_e$ of conductive heat transfer that is used to infer χ_e^{exp}. An alternative form[29] of the effective paleoclassical thermal diffusivity can be constructed using the paleoclassical heat transport operator in analogy to the procedure used to construct χ_e^{exp}

$$(\chi_{ePB}^{\text{paleo}})_{\text{eff}} = \frac{P_e^{\text{paleo}}(\rho)}{n_e T_e\frac{V'}{(\bar{a})^2}aL_{Te}^{-1}}, \tag{35}$$

where $\bar{a}=a(2\kappa^2/1+\kappa^2)$,

$$P_e^{pc}(\rho_i) = -\int_0^{\rho_i} d\rho(1+M)\frac{\partial^2}{\partial\rho^2}\left(V'\frac{D_\eta}{(\bar{a})^2}\frac{3}{2}nT\right) \equiv -\int_0^{\rho_i} d\rho(1+M)\frac{\partial^2}{\partial\rho^2}\left(\rho\widehat{D}_\eta\frac{n}{T^{1/2}}\right) \tag{36}$$

is the radial paleoclassical heat flow through the flux surface at $\rho_i=r/a$,

$$D_\eta = \frac{1400Z_{\text{eff}}}{T_e^{3/2}}\left(\frac{\ln\Lambda}{17}\right)\frac{\eta_\parallel}{\eta_0} \tag{37}$$

is the magnetic field diffusivity, and $V'=(2\pi a)^2\kappa R\rho(1+1/2\rho\partial\ln\kappa/\partial\rho)$. Here, κ is the elongation.

2. Electron temperature gradient modes

The electron temperature gradient (ETG) modes are electrostatic drift waves with $k_\perp c_s \leqslant \omega_{pe}$. The threshold electron temperature gradient for the linear destabilization of ETG modes has been established from linear toroidal gyrokinetic simulations[11]

$$\left(\frac{R}{L_{Te}}\right)_{\text{crit}} = \max\left[\begin{array}{l}0.8R/L_{ne}, \text{ or}\\ (1+\tau)\left(1.33+1.91\frac{r}{q^2}\frac{dq}{dr}\right)(1-1.15\varepsilon)\end{array}\right]. \tag{38}$$

For $R/L_{Te} < (R/L_{Te})_{\text{crit}}$, the toroidal ETG modes are linearly stable, but for $R/L_{Te} > (R/L_{Te})_{\text{crit}}$ the modes would be expected to exist and produce transport.

A simple expression for the thermal conductivity due to the ETG modes is given by[9]

$$\chi_e^{\text{ETG}} = 0.13\left(\frac{c_s}{\omega_{pe}}\right)^2\frac{v_{\text{the}}S_m}{qR}\eta_e(1+\eta_e), \tag{39}$$

where $S_m \equiv (r/q)(dq/dr)$ is the magnetic shear and ω_{pe} is the electron plasma frequency.

The short-wavelength ETG modes are not thought to be strongly affected by $E\times B$ flow shear.[19] However, shear also produces a shift of the drift wave eigenmodes off the rational surface and a twisting of mode structure, which suppresses the turbulent transport due to ETG modes.[30] This suppression can be represented by the multiplicative suppression factor[19,30]

$$F_s^{\text{ETG}} = \frac{1}{1+(Y_s^{\text{ETG}})^2}, \quad Y_s = \sqrt{\frac{m_i}{T_e}}\left|\frac{R\frac{\partial}{\partial r}\left(\frac{E_r}{RB_\theta}\right)}{\frac{1}{q}\frac{\partial q}{\partial r}}\right| \tag{40}$$

and the shear-suppressed ETG mode thermal diffusivity can be represented as

$$\hat{\chi}_e^{\text{ETG}} = F_s^{\text{ETG}}\chi_e^{\text{ETG}}. \tag{41}$$

A recent development by Horton *et al.*[13] includes the magnetic shear suppression directly in the derivation

$$\chi_e^{\mathrm{ETG}} = C_e^{es} q^2 \left(\frac{R}{L_{Te}}\right)^{3/2} \left(\frac{\rho_e^2 v_{\mathrm{the}}}{T_e}\right) \left[-\nabla T_e - 1.88 \left(\frac{|S_m| T_e}{qR}\right) \times \left(1 + Z_{\mathrm{eff}} \frac{T_e}{T_i}\right)\right], \quad \ell_{c,e}^{es} \geq \delta_e$$
$$= C_e^{es} \left(\frac{c^2}{\omega_{pe}^2}\right) \left(\frac{v_{\mathrm{the}}}{\sqrt{RL_{Te}}}\right), \quad \ell_{c,e}^{es} < \delta_e \tag{42}$$

where C_e^{es} is a parameter, interpreted as the fraction to which the turbulence reaches the unsuppressed level, which must be fitted to match experimental data (Horton *et al.*[13] found $C_e^{es} \approx 0.03$ for Tore Supra, and Bateman *et al.*[31] use $C_e^{es} \approx 0.06$ in their Multimode transport model), $\ell_{c,e}^{es} = q\rho_e R / L_{Te}$, and δ_e is the collisionless skin depth.

3. Trapped electron modes

The principal electron drift instabilities with $k_\perp c_s \leq \Omega_i$ arise from trapped particle effects when $\nu_e^* \equiv \nu_e / (v_{\mathrm{the}}/qR)\varepsilon^{3/2} < 1$. In more collisional plasmas the mode becomes a collisional drift wave destabilized by passing particles. A simple expression for the electron heat diffusivity associated with electron trapping was given by Kadomtsev and Pogutse[32] based on the improved mixing length estimate $\chi \approx (\gamma^3 / k_{\mathrm{TEM}}^2)/(\gamma^2 + \omega_r^2)$,

$$\chi_e^{\mathrm{TEM}} = \frac{f_{\mathrm{tr}} \eta_e \rho_i^2 \omega_{*e}^2 (\nu_e/\varepsilon)}{\omega_{*e}^2 + (\nu_e/\varepsilon)^2}, \tag{43}$$

where $k_{\mathrm{TEM}} \simeq 1/\rho_i$, the value of the TEM k-value for which the maximum growth rate occurs, has been used.

Weiland[15] considers a reactive trapped electron mode which is almost symmetric to the ITG mode leading to the transport given by Eqs. (12a) and (12b). The improved mixing length quasilinear estimate of the effective electron heat diffusivity of this coupled term is

$$(\chi_e^{\mathrm{TEM}})_{\mathrm{eff}} = \frac{f_{\mathrm{tr}}}{\eta_e} \left(\eta_e - \frac{2}{3} - \frac{2}{3}\Delta_e\right) \frac{\gamma^3/k^2}{\left(\omega_r - \frac{5}{3}\omega_{De}\right)^2 + \gamma^2}, \tag{44}$$

where

$$\Delta_e = \frac{1}{N} \left\{ |\hat{\omega}|^2 \left[|\hat{\omega}|^2 (\varepsilon_n - 1) + \hat{\omega}_r \varepsilon_n \left(\frac{14}{3} - 2\eta_e - \frac{10}{3}\varepsilon_n\right) + \frac{5}{3}\varepsilon_n^2 \left(-\frac{8}{3} + 3\eta_e + \frac{2}{3}\varepsilon_n\right)\right] - \frac{50}{9}\hat{\omega}_r \varepsilon_n^3 (1 - \varepsilon_n) + \frac{25}{9}\left(\frac{7}{3} - \eta_e - \frac{5}{3}\varepsilon_n\right)\right\} \tag{45}$$

and the other quantities are defined above in the section on ITG modes.

The TEMs are longer wavelength modes coupled to the ITG modes and should be suppressed by $E \times B$ flow shear in the same way as the ITG modes, so that the $E \times B$ shear-suppressed thermal diffusivity due to TEMs can be represented as[19]

$$\hat{\chi}_e^{\mathrm{TEM}} = F_s^{\mathrm{ITG}} \chi_e^{\mathrm{TEM}} \tag{46}$$

and the further magnetic suppression is represented as for the ITG modes

$$\tilde{\chi}_e^{\mathrm{TEM}} = G(S_m) \hat{\chi}_e^{\mathrm{TEM}} = G(S_m) F_s^{\mathrm{ITG}}(\omega_{E\times B}) \chi_e^{\mathrm{TEM}}. \tag{47}$$

4. Drift resistive ballooning mode

The drift-resistive ballooning (DRB) mode is destabilized by unfavorable curvature on the outboard side of the torus in a collisional edge plasma. Linear stability analysis[33] indicates that the transport associated with these modes can be characterized by a particle diffusion coefficient scaling $D \sim (2\pi q)^2 \rho_e^2 \nu_{ie} (R/L_n)$ with a proportionality constant equal to the flux surface average of the normalized fluctuating radial particle flux $\langle nV_r \rangle$. Subsequent calculations[34] found robust growth rates of DRB modes for the edge parameters of DIII-D and predicted the normalized fluctuating radial particle fluxes for models representative of DIII-D core parameters $\langle nV_r \rangle \approx 0.01 - 0.05$. We adopt the form

$$\chi_e^{\mathrm{DRB}} = 4 \frac{R}{L_n} (q\rho_e)^2 \nu_e \tag{48}$$

with the normalization factor equal to 4 to characterize the transport of electron energy due to drift-resistive ballooning modes, with the caveat that there could well be an additional normalization constant needed. We note that one group of transport modelers[35] calibrated this formula to L-mode data and found a factor of $94\kappa^{-4}$ (instead of 4) should multiply this expression (κ is the elongation), while another group[16] used this expression with the factor of 4.

The $E \times B$ flow shear suppression for DRB modes is represented[19] by the multiplicative factor

$$F_s^{\mathrm{DRB}} = \frac{1}{1 + (Y_s^{\mathrm{DRB}})^2},$$
$$Y_s^{\mathrm{DRB}} = \omega_{E\times B} \tau_{\mathrm{DRB}} = \omega_{E\times B} \left(\frac{L_{\mathrm{DRB}}^2}{\chi_e^{\mathrm{DRB}}}\right), \tag{49}$$
$$L_{\mathrm{DRB}} = 2\pi q \left(\frac{2ne^2 \eta_\parallel \rho_i}{m_e \Omega_e \sqrt{2RL_n}}\right)$$

where the expression for the correlation length (turbulence characteristic scale length) L_{DRB} is taken from Ref. 36. The $E \times B$ shear-suppressed thermal diffusivity is then represented as

$$\hat{\chi}_e^{\mathrm{DRB}} = F_s^{\mathrm{DRB}} \chi_e^{\mathrm{DRB}}, \tag{50}$$

and the additional magnetic shear suppression is represented by

$$\tilde{\chi}_e^{\mathrm{DRB}} = G(S_m) \hat{\chi}_e^{\mathrm{DRB}} = G(S_m) F_s^{\mathrm{DRB}} \chi_e^{\mathrm{DRB}}. \tag{51}$$

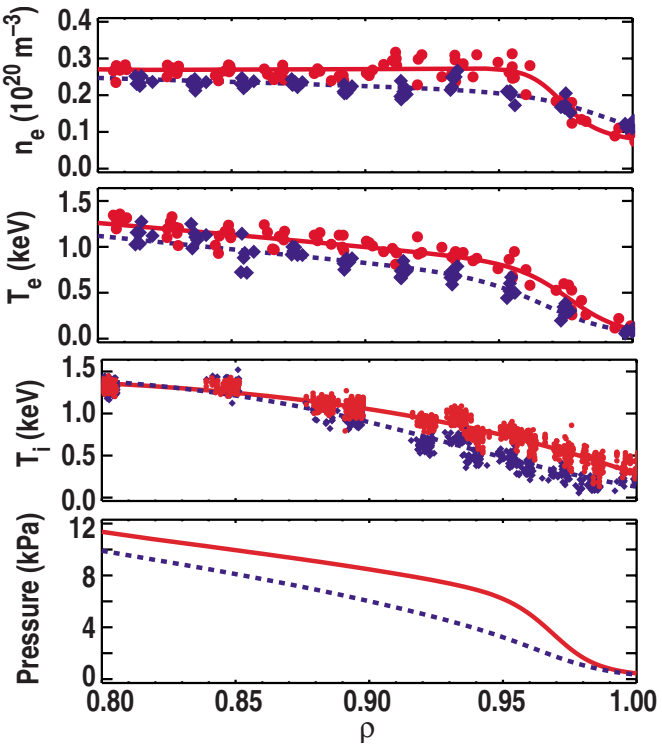

FIG. 1. (Color online) Density, temperatures, and pressure in edge region of DIII-D shot 119436 (squares=data 10%–20% after ELM crash, +=data 80%–99% after ELM crashes used in the analyses of this paper, dashed line=fit 10%–20% after ELM crash, solid line=fit 80%–99% after ELM crashes) ρ=normalized radius (see Ref. 5).

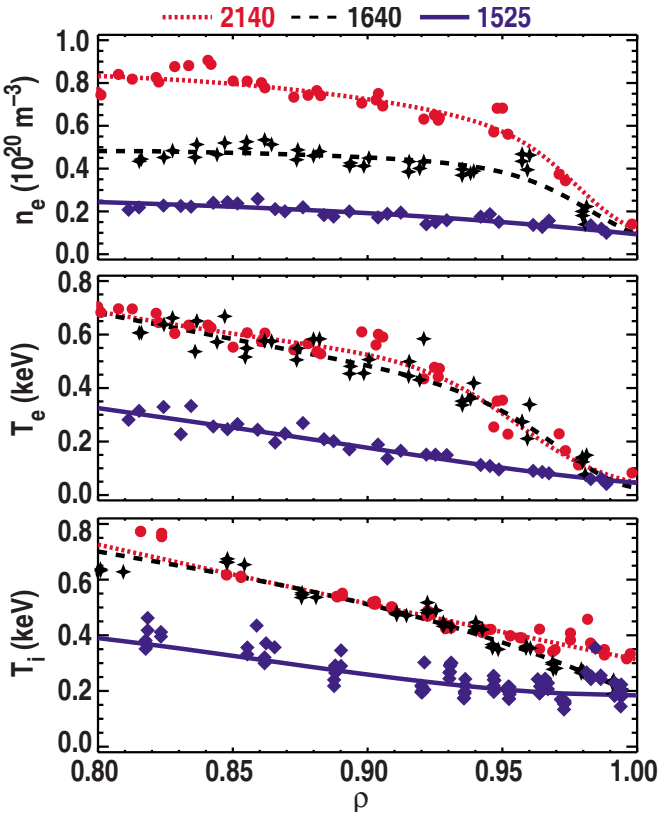

FIG. 2. (Color online) Measured and fitted densities and temperatures in the edge of DIII-D shot 118897 during the ELM-free phase (Ref. 4) (L-H transition took place just before 1640 ms).

5. Resonant magnetic perturbation diffusion

When the I-coil is turned on (in DIII-D) there is a resonant magnetic perturbation in the plasma edge in DIII-D. A magnetic field line integration code[37] is used to numerically calculate the magnetic diffusivity D_m across the outer region of the plasma where resonant magnetic perturbations from the DIII-D I-coil are expected to produce a significant level of stochasticity. The magnetic diffusivity of a field line is defined as

$$D_m = \delta r^2/2L, \tag{52}$$

where δr is the total radial displacement, calculated at the outboard midplane, between the starting point of the field line calculation and its end point. Here, L is the total parallel field line length from the starting point to the end point. Since the DIII-D version of the field line integration code calculates trajectories in poloidal flux space (ψ), an average D_m^{ψ} taken over an ensemble of N starting points on a single flux surface is determined on each flux surface based on the diffusion field lines in flux space using

$$\langle D_m^{\psi} \rangle = \frac{1}{N} \sum_{j=1}^{N} \delta\psi_j^2/2L_j, \tag{53}$$

where $\delta\psi_j$ is the total displacement of a single field line in poloidal flux and L_j is its total parallel length. As discussed in Ref. 38, $\langle D_m^{\psi} \rangle$ is converted to real space variables $\langle D_m^r \rangle$ with units of meters using a geometric factor that accounts for the shape of the flux surface. Then, an average stochastic magnetic electron thermal diffusivity $\langle \chi_{e-m}^r \rangle$ in units of m^2/s is calculated using

$$\langle \chi_{e-m}^r \rangle = v_{\text{the}} \langle D_m^r \rangle, \tag{54}$$

where v_{the} is the electron thermal speed on the starting flux surface. The code is typically set to calculate N=180 poloidally distributed, equally spaced, field line trajectories on each flux surface and follows each field line until it either hits a solid surface or makes 200 toroidal revolutions. A field line escape fraction f_{esc}, the ratio of field lines hitting a solid surface to the number of field lines started on each flux surface N, is calculated on each flux surface and a weighted $\langle \chi_{e-m}^r \rangle_w$ is calculated using

$$\langle \chi_{e-m}^r \rangle_w = f_{\text{esc}} \langle D_m^r \rangle. \tag{55}$$

III. EVALUATION OF EXPERIMENTAL HEAT DIFFUSIVITIES

Since the total ion and electron heat fluxes, $Q_{i,e}$, consist of a conductive component $q_{i,e}=-\chi_{i,e} n \nabla T_{i,e}=\chi_{i,e} n T_{i,e} L_{Ti,e}^{-1}$ plus a convective component $5/2\Gamma_{i,e}T_{i,e}$, values for the radial thermal diffusivities can be inferred from the experimental density and temperature profiles using[2–5]

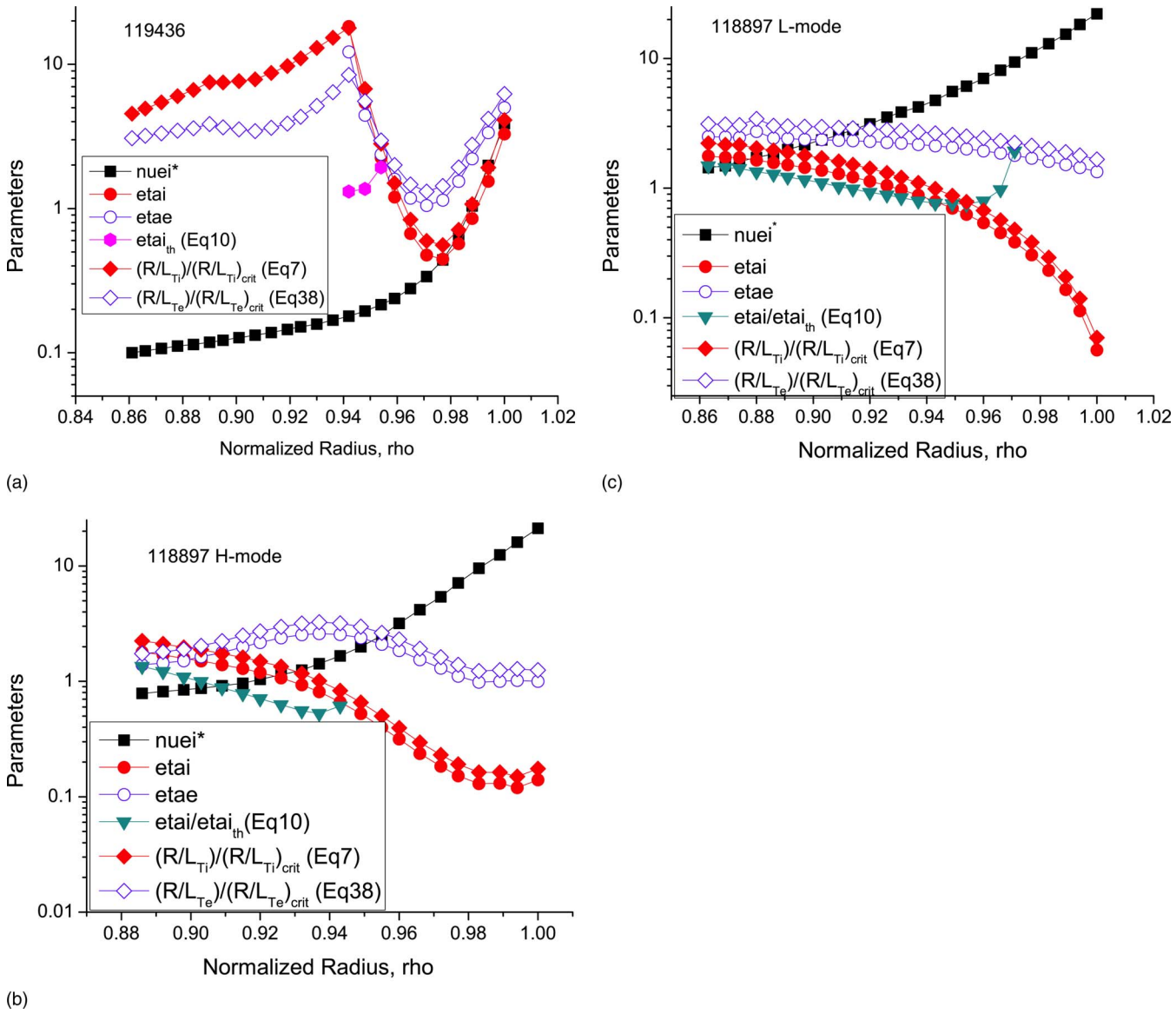

FIG. 3. (Color online) Transport parameters ν_{ei}^{*}, $\eta_{i,e}\equiv L_n/L_{Ti,e}$, $\eta_i/\eta_{\mathrm{ITH}}$, $(R/L_{Ti,e})/(R/L_{Ti,e})_{\mathrm{crit}}$ in the edge of (a) ELMing H-mode shot 119436, (b) ELM-free H-mode shot 118897 at 2140 ms, (c) L-mode shot 118897 at 1525 ms.

$$\chi_{i,e}^{\exp}(r)=L_{Ti,e}(r)\frac{q_{i,e}(r)}{n_{i,e}(r)T_{i,e}(r)} \equiv L_{Ti,e}(r)\left[\frac{Q_{i,e}(r)}{n_{i,e}(r)T_{i,e}(r)}-\frac{5}{2}\frac{\Gamma_{i,e}(r)}{n_{i,e}(r)}\right], \tag{56}$$

where $L_{Ti,e}^{-1}\equiv-(\partial T_{i,e}/\partial r)/T_{i,e}$, $Q_{i,e}$ are the total heat fluxes, which satisfy

$$\frac{\partial Q_i}{\partial r}=-\frac{\partial}{\partial t}\left(\frac{3}{2}n_iT_i\right)+q_{nbi}-\frac{3}{2}(T_i-T_o^c)n_in_o^c\langle\sigma v\rangle_{\mathrm{cx+el}} -q_{ie},\quad Q_i(r_{\mathrm{sep}})=Q_{\mathrm{sep}i}^{\exp} \tag{57}$$

and

$$\frac{\partial Q_e}{\partial r}=-\frac{\partial}{\partial t}\left(\frac{3}{2}n_eT_e\right)+q_{nbe}+q_{ie}-n_en_o\langle\sigma v\rangle_{\mathrm{ion}}E_{\mathrm{ion}} -n_en_zL_z,\quad Q_e(r_{\mathrm{sep}})=Q_{\mathrm{sep}e}^{\exp} \tag{58}$$

and $\Gamma_{i,e}\equiv n_{i,e}v_{ri,e}$ is the radial particle flux, which satisfies

$$\frac{\partial\Gamma_i}{\partial r}=-\frac{\partial n_i}{\partial t}+n_en_o\langle\sigma v\rangle_{\mathrm{ion}}+S_{nb},\quad \Gamma_i(r_{\mathrm{sep}})=\Gamma_{\mathrm{sep}i}^{\exp}. \tag{59}$$

In these equations, n_o is the recycling or gas fueling neutral density in the edge pedestal (the superscript c denotes uncollided "cold" neutrals), $q_{\mathrm{nbi},e}$ is the neutral beam heating, S_{nb} is the neutral beam particle source, q_{ie} is the collisional energy transfer from ions to electrons, $\langle\sigma v\rangle_x$ is an atomic physics reaction rate (x=cx+el denotes charge-exchange plus elastic scattering, x=ion denotes ionization), n_z and L_z are the impurity density and radiation emissivity, and E_{ion} is the

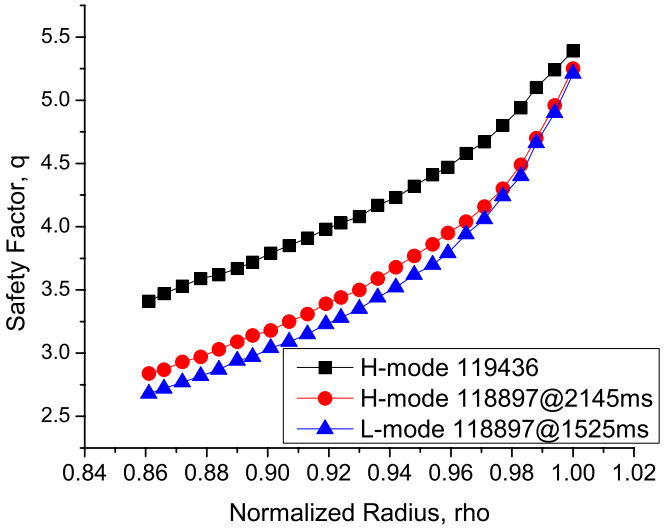

FIG. 4. (Color online) Safety factor in edge plasmas.

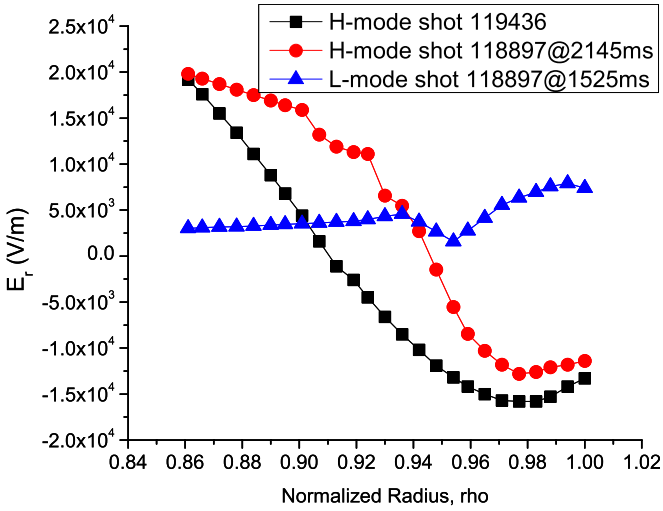

FIG. 5. (Color online) Radial electric field.

ionization potential. The atomic physics data are taken from Ref. 39, and the radiation emissivity is calculated from a fit to coronal equilibrium calculations (taking into account the effect of charge-exchange and recombination in the presence of recycling neutrals) based on the data given in Ref. 40.

The experimental heat diffusivity of Eq. (56) is the proper quantity to compare with theoretical predictions of the actual conductive heat diffusivity, such as the neoclassical prediction of Eq. (1). However, many of the expressions for the heat diffusivities due to turbulence were constructed by dividing the theoretical expression for the total ion or electron heat flux due to turbulence by the corresponding temperature gradient and density (i.e., the total heat flux was effectively assumed to be conductive, and any convective heat flux was neglected). Such theoretical expressions should probably be compared with an effective experimental heat diffusivity constructed in a similar fashion

$$(\chi_{i,e}^{\exp})_{\text{eff}} = L_{Ti,e}(r)\frac{Q_{i,e}(r)}{n_{i,e}(r)T_{i,e}(r)}. \tag{60}$$

This effective quantity should be interpreted as just what it is, a ratio of total heat flux to the product of the density and the temperature gradient, and not attributed any physical significance as a "heat diffusivity."

An integrated modeling code[41] was used to i) calculate particle and power balances on the core plasma in order to determine the net particle and heat outfluxes from the core into the scrape-off layer (SOL), which are input to ii) an extended 2-point divertor plasma model (with radiation and atomic physics) that calculated densities and temperatures in the SOL and divertor and the ion flux incident on the divertor plate, which iii) was recycled as neutral atoms and molecules that were transported through the 2D divertor region across the separatrix to fuel the core plasma.

Equations (57)–(59) were integrated over the edge region to calculate the heat and particle flux profiles, using the experimental density and temperature profiles. The separatrix boundary conditions on the particle and heat fluxes were the "steady-state" experimental values determined from the integrated modeling code. The time derivative terms were evaluated from experimental data to account for plasma heating, etc. The heat and particle fluxes calculated from Eqs. (57)–(59) were then used, together with the experimental density and temperature profiles, to infer the experimental thermal diffusivities from Eq. (56). The details of this procedure and the uncertainties in the resulting experimental thermal diffusivities are described in previous papers.[2–5]

IV. DIII-D SHOTS 119436 AND 118897

Two DIII-D shots for which detailed data analysis had been previously performed[4,5] were selected for comparison of theoretically predicted and experimentally inferred heat diffusivities. In both shots the experimental data were analyzed over about the outer 15% of the plasma radius, including both the steep-gradient edge pedestal region and the relatively flat density and temperature "flattop" region just inside the edge pedestal. Both shots were lower single null divertor configuration with neutral beam heating.

Shot 119436 was an ELMing H-mode shot with a global steady state phase, which was analyzed. To reduce the influence of any random measurement errors, the time interval between ELMs was divided into 5 time bins, and data was collected from a sequence of inter-ELM time intervals and averaged, as indicated in Fig. 1 and described in detail in Ref. 5. The data in the time bin just before an ELM crash was chosen for the analyses of this paper. The main parameters were $B=-1.64$ T, $I=0.99$ MA, $R=1.77$ m, $a=0.58$ m, $\kappa=1.83$. The time 3250 ms was chosen for analysis. At this time the neutral beam power was 4.3 MW, the gas fueling rate was 0 atoms/s, the line average density was $\bar{n}=4.2\times10^{19}/\text{m}^3$, and the safety factor was $q_{95}=4.2$. The parameters at the top of the edge pedestal were $n_{\text{ped}}=1.8\times10^{19}/\text{m}^3$, $T^i_{\text{ped}}=731$ eV, $T^e_{\text{ped}}=900$ eV.

Shot 118897 had an ELM-free L-mode and H-mode phase, both of which were analyzed for this paper. The edge density and temperature measurements for three times in the ELM-free phase of this shot are shown in Fig. 2. The main parameters were $B=-1.98$ T, $I=1.39$ MA, $R=1.71$ m,

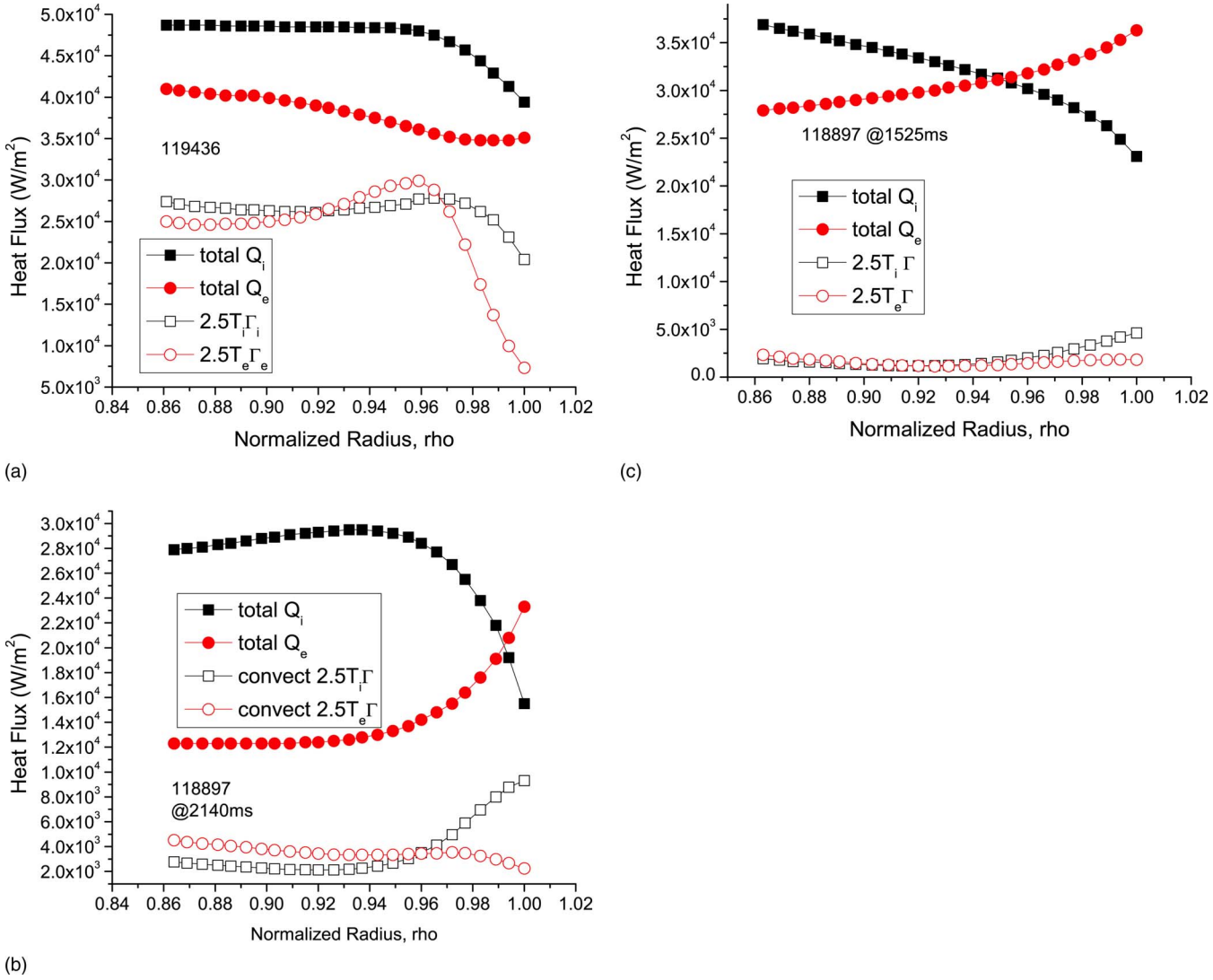

FIG. 6. (Color online) Heat fluxes in DIII-D (a) ELMing H-mode shot 119436, (b) ELM-free H-mode shot 118897 at 2140 ms, (c)L-mode shot 118897 at 1525 ms.

$a=0.60$ m, $\kappa=1.82$. The L-H transition occurred shortly after the time, 1525 ms, chosen for analysis of the L-mode. At this time the neutral beam power was 4.45 MW, the gas fueling rate was 6.2×10^{19} atoms/s, the line average density was $\bar{n}=3.2\times10^{19}/\mathrm{m}^3$, and the safety factor was $q_{95}=3.52$. The parameters at the top of the edge pedestal were $n_{\mathrm{ped}}=1.16\times10^{19}/\mathrm{m}^3$, $T^i_{\mathrm{ped}}=200$ eV, $T^e_{\mathrm{ped}}=50$ eV. The time chosen for the H-mode analysis, 2140 ms, was well after the L-H transition and before the first ELM occurred. At this time the neutral beam power was 2.33 MW, the gas fueling rate was 2.5×10^{19} atoms/s, the line average density was $\bar{n}=7.7\times10^{19}/\mathrm{m}^3$, and the safety factor was $q_{95}=3.70$. The parameters at the top of the edge pedestal were $n_{\mathrm{ped}}=8.03\times10^{19}/\mathrm{m}^3$, $T^i_{\mathrm{ped}}=694$ eV, $T^e_{\mathrm{ped}}=524$ eV.

The data analysis procedure is described in Refs. 4 and 5. The details of the data interpretation procedure described in the previous section for these shots are also described in Refs. 4 and 5, where uncertainties in the evaluation of thermal diffusivities from the measure density and temperature profiles and the treatment of transient conditions are also discussed in detail.

V. COMPARISON OF THEORETICAL AND EXPERIMENTAL HEAT DIFFUSIVITIES

A. Transport parameters

Various parameters which affect the theoretical transport predictions are shown in Fig. 3. Shot 119436 was the least collisional, with the collisionality parameter ν^*_{ei} varying monotonically from about 0.1 in the inner flattop region (at $\rho\simeq0.86$) to about 3.0 just inside the separatrix (at $\rho=1$). For the H-mode phase of shot 118897 the corresponding variation in ν^*_{ei} was from about 0.8 to about 20, and for the L-mode phase of shot 118897 the corresponding variation in ν^*_{ei} was from about 1.1 to about 25.

The parameter $\eta_{i,e}\equiv L_n/L_{Ti,e}\equiv(-dn/ndr)/(-dT_{i,e}/T_{i,e}dr)$ is everywhere greater than unity for electrons in both the L- and H-mode phases of shot 118897 and greater than unity for $\rho>0.94$ in shot 119436, which is sometimes taken as an indication of the instability of ETG modes and the presence of ETG transport. This parameter for ions is larger than unity (taken as an indication of the existence of ITG transport) for the flattop region but

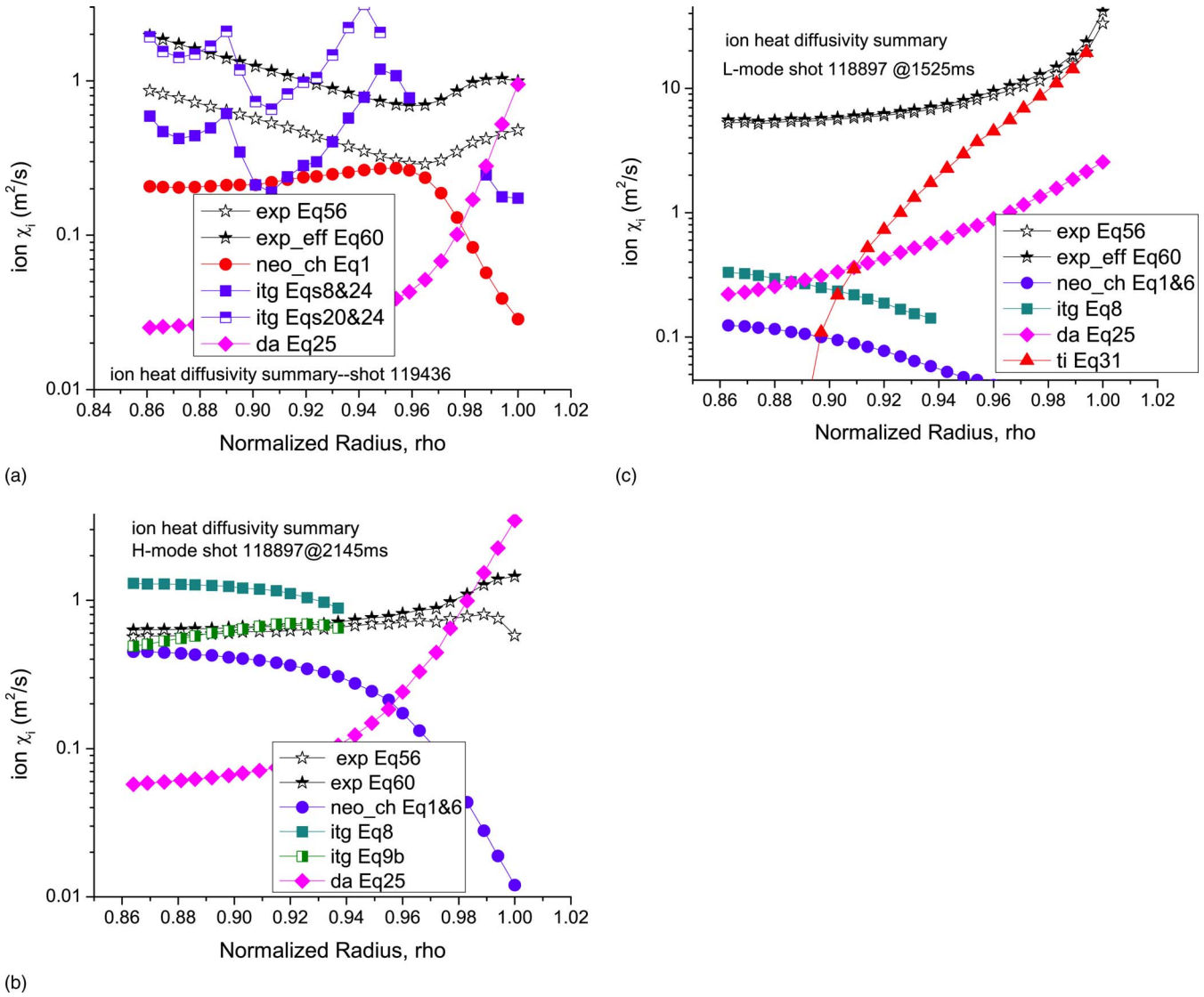

FIG. 7. (Color online) Summary of ion heat diffusivity comparison of theory with experiment for DIII-D (a) ELMing H-mode shot 119436, (b) ELM-free H-mode shot 118897 at 2140 ms, (c) L-mode shot 118897 at 1525 ms.

smaller than unity for the steep-gradient pedestal region for both the L- and H-mode phases of shot 118897. The behavior of this parameter in shot 119436 is interesting in that the density profile was actually slightly hollow, inside of $\rho \approx 0.94$, leading to $L_n \equiv -n/(dn/dr) < 0$ over the flattop region. This in turn led to $\eta_{i,e} \equiv L_n/L_{Ti,e} < 0$ over the flattop region, which in turn led to negative heat diffusivities or other unphysical behavior being predicted by some of the theoretical formulas.

The temperature gradient conditions for the onset of ETG instabilities (hence the existence of ETG transport) given by Eq. (38), $[R/L_{Te} > (R/L_{Te})_{\mathrm{crit}}]$ was satisfied over the entire domain $0.86 < \rho < 1.0$ for all three shots. The corresponding condition for the onset of ITG instabilities (hence for the existence of ITG transport) given by Eq. (7), $[R/L_{Ti} > (R/L_{Ti})_{\mathrm{crit}}]$, was generally satisfied in the flattop region for all shots and just inside the separatrix for shot 119436, but was not satisfied in general in the steep-gradient edge pedestal region.

The evaluation of the instability threshold condition for ITG-TEM modes in the Weiland model, Eq. (10), yielded essentially the same results as the $[R/L_{Ti,e} > (R/L_{Ti,e})_{\mathrm{crit}}]$ criteria for the L- and H-mode phases of shot 118897. However, the evaluation of Eq. (10) for shot 119436 led to negative values for $\rho \geqslant 0.96$ and for $\rho \leqslant 0.94$. The negative values of Eq. (10) for $\rho \geqslant 0.96$ can be interpreted as ITG instability for any $\eta_i > 0$, which then makes the prediction of ITG instability and transport for $\rho \geqslant 0.94$ consistent with the $[R/L_{Ti} > (R/L_{Ti})_{\mathrm{crit}}]$ prediction for shot 119436. However, for $\rho \leqslant 0.94$, the hollow density profile leads also to $\eta_i < 0$, making the evaluation of ITG instability and the existence of ITG and TEM transport from Eq. (10) indeterminate for this model in this region.

The profiles of the safety factor and of the radial electrical field are important for the evaluation of theoretical expressions for the magnetic and $E \times B$ shear, for the evaluation of the orbit squeezing and loss fraction corrections, and for the evaluation of transport coefficients depending on q.

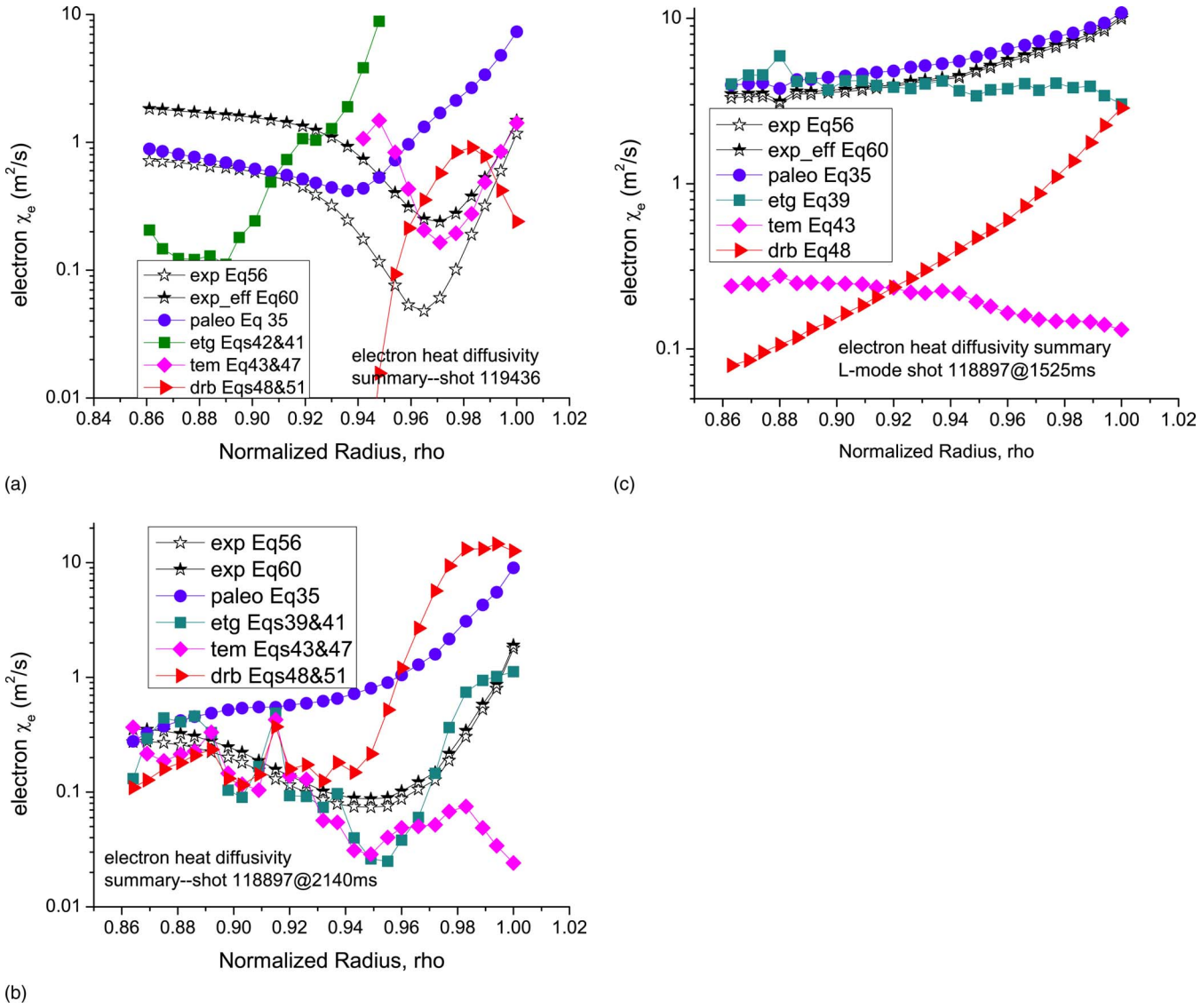

FIG. 8. (Color online) Comparison of theoretical and experimental electron heat diffusivities for DIII-D (a) ELMing H-mode shot 119436, (b) ELM-free H-mode shot 118897 at 2140 ms, (c) L-mode shot 118897 at 1525 ms.

Experimental profiles for these quantities are shown in Figs. 4 and 5. The discontinuous fits to the discrete E_r data points introduces spurious structure into the evaluation of dE_r/dr from the experimental data needed for the $E \times B$ shear correction factor.

B. Calculation of heat fluxes and inference of heat diffusivities

The experimental data were used to evaluate the heating and cooling rates and the particle sources in Eqs. (57)–(59) and these equations were integrated inward from experimental separatrix boundary conditions to obtain the total and convective heat fluxes shown in Fig. 6. Details of this procedure are discussed in Refs. 2–5. These heat fluxes were then used, together with the experimental density and temperature data, to evaluate Eqs. (56) and (60) in order to infer the experimental heat diffusivities. We note that a more accurate determination of the experimental time derivatives of density and energy has become available for shot 118897 since Ref. 4 was published, so that the heat fluxes and consequently the inferred experimental heat diffusivities of this paper differ somewhat from those in Ref. 4.

As discussed previously, the heat diffusivity is understood as being associated with the conductive heat flux, and Eq. (56) is the consistent relationship for its evaluation. However, since many theoretical expressions for the heat diffusivity are derived by dividing the theoretical prediction for the total heat flux by the temperature gradient (and density), Eq. (60) provides a better quantity for comparison with theory in those cases. In shot 118897 the convective heat flux is relatively small except just inside the separatrix in the H-mode phase, and there is no practical difference between Eqs. (56) and (60), but for H-mode shot 119436, the convective heat flux is substantial over the entire edge region and there is a significant difference between the heat diffusivities inferred from the two equations.

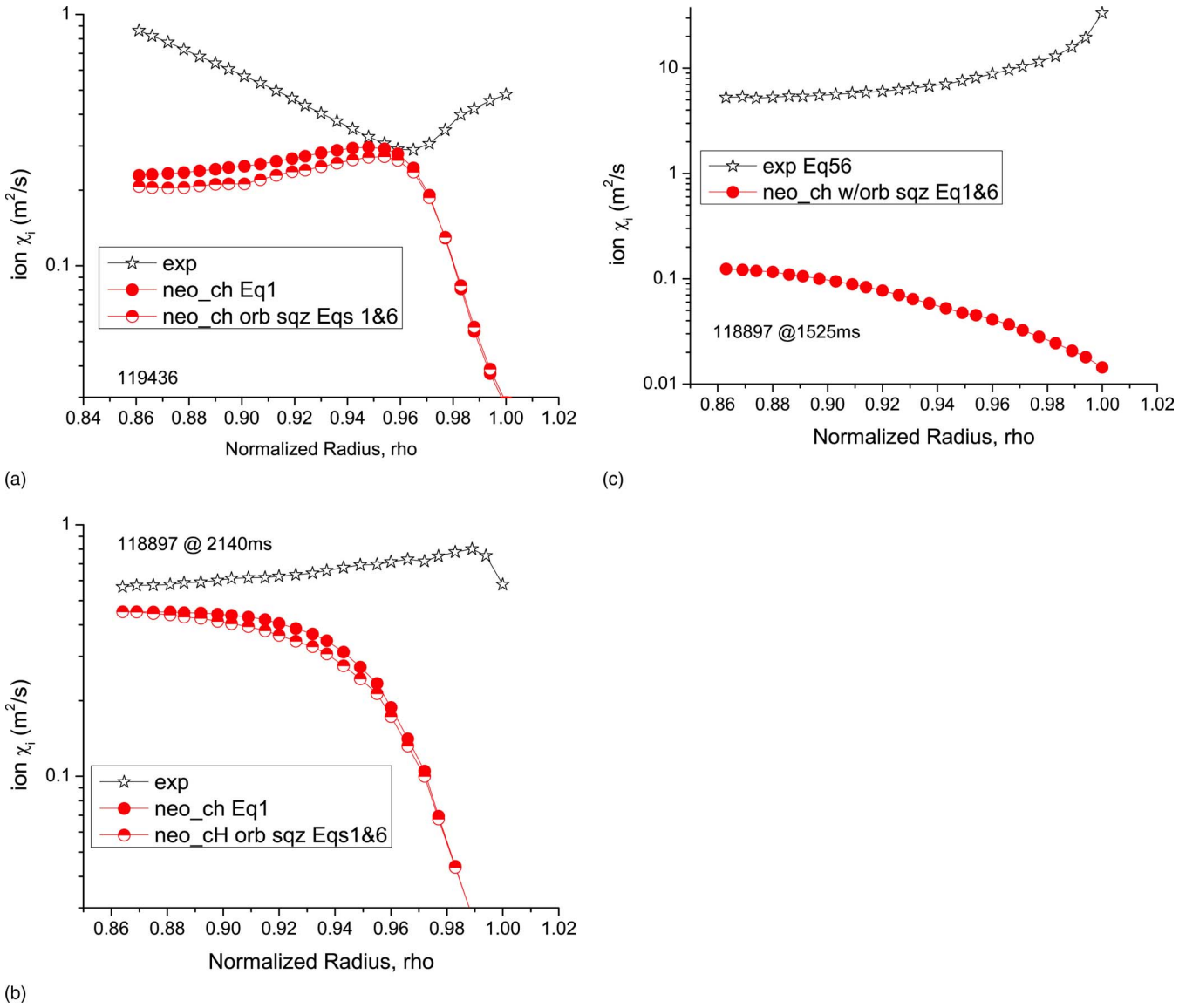

FIG. 9. (Color online) Neoclassical Chang–Hinton [Eq. (1)] prediction compared with experiment [Eq. (56)] for DIII-D (a) ELMing H-mode shot 119436, (b) ELM-free H-mode shot 118897 at 2140 ms, (c) L-mode shot 118897 at 1525 ms.

C. Comparison of theoretical and experimental heat diffusivities

A detailed comparison of the predictions of all of the heat diffusivity models of Sec. II with the experimentally inferred heat diffusivities is described in the Appendix. This comparison, as it pertains to providing insight as to which heat transport mechanisms are the more promising for explaining the inferred experimental heat diffusivities, is summarized in this section. When a prediction is shown only over part of the edge region this is because either the existence condition [e.g., Eqs. (7) and (10) or (38)] is not satisfied, the formula gave unphysical results [e.g., the hollow density profile in the flattop of shot 119436 led to $L_n<0$ and hence $\eta_{i,e}<0$, causing predictions of negative heat diffusivities by formulas such as Eq. (39) for ETG, Eq. (43) for TEM, and Eq. (48) for DRB], or the evaluation of involved expressions [e.g., Eqs. (12a), (12b), and (13)–(19) for ITG] simply broke down for the parameters of the plasma edge. These problems are discussed in the Appendix.

Summary of ion heat diffusivity comparison: A comparison of the ion heat diffusivities predicted by the neoclassical (neo_ch) model, by two of the ion temperature gradient (ITG) mode models, and by the drift Alfvén (da) model are collected in Fig. 7, where the experimentally inferred heat diffusivities are also shown. Also included is the thermal instability (ti) model prediction for the L-mode phase of shot 118897; the prediction for the H-mode shots was no thermal instability. For shot 119436, two ITG mode calculations, Eqs. (8) and (20), are shown, both with $E\times B$ and magnetic shear suppression. No $E\times B$ shear suppression is included in the drift Alfvén mode calculation (because numerical modeling[25] indicates that it is ineffective) nor, of course, in the neoclassical calculation. It is apparent from Figs. 7(a) and 7(b) that some combination of the neoclassical, drift Alfvén, and the ITG heat diffusivities could provide a reasonably good match to the experimental ion heat diffusivity for the two H-mode shots, which suggests that these three ion heat transport mechanisms should receive attention in

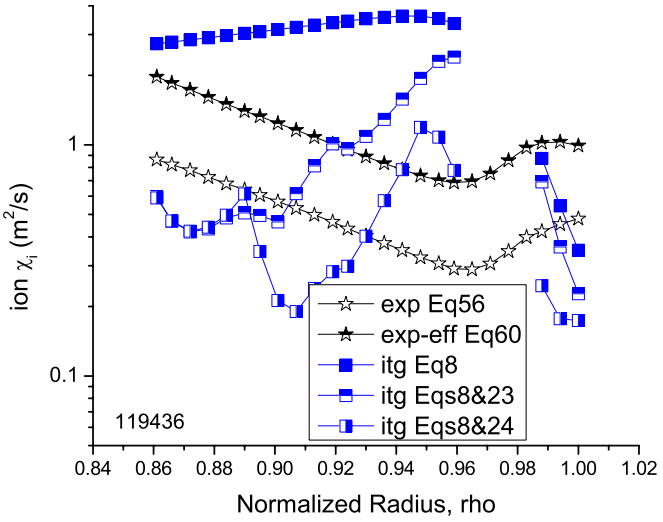

FIG. 10. (Color online) Comparison of ITG prediction of Eq. (8) with experimental ion heat diffusivity, with and without $E\times B$ and magnetic shear suppression for DIII-D ELMing H-mode shot 119436.

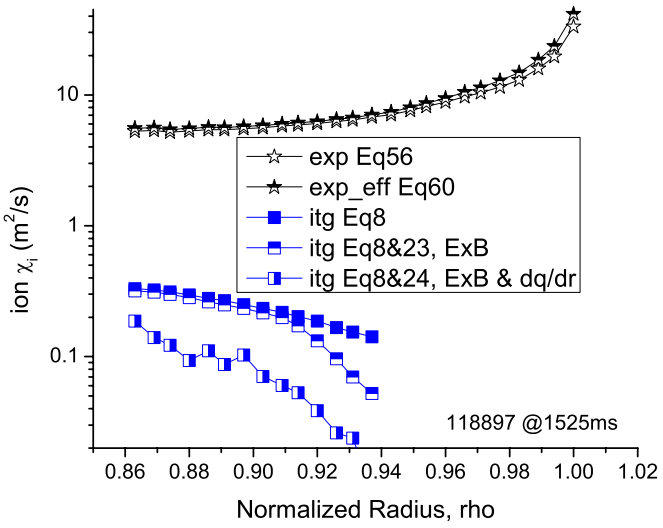

FIG. 12. (Color online) Comparison of ITG prediction of Eq. (8) with experimental ion heat diffusivity, with and without $E\times B$ and magnetic shear suppression for DIII-D ELM-free L-mode shot 118897.

future investigations. All of the theories substantially underpredict the experimental heat diffusivities in the L-mode shot, except the thermal instability (ti) theory just inside the separatrix where the radiative instability growth rates are the largest.

Summary of electron heat diffusivity comparison: A comparison of the electron heat diffusivities predicted by the paleoclassical (paleo) model, by the electron temperature gradient (ETG) mode model, by the trapped electron mode (TEM) model, and by the drift resistive ballooning mode (DRB) model are collected in Fig. 8, where the experimentally inferred heat diffusivities are also shown. The TEM and DRB heat diffusivities shown for the H-mode shots are $E\times B$ and magnetic shear suppressed. The paleoclassical prediction is in reasonable agreement with experiment in the flattop region, but overpredicts it in the steep-gradient region, for the H-mode shots [Figs. 8(a) and 8(b)]. However, the paleoclassical prediction is in excellent agreement with experiment for the L-mode phase of shot 118897 [Fig. 8(c)]. The ETG prediction is in reasonable agreement with experiment in both H-mode shots and in the L-mode shot. The TEM predictions agree reasonably well in radial profile and magnitude with experiment for the H-mode shots [Figs. 8(a) and 8(b)], but substantially underpredict the experiment in the L-mode phase of shot 118897 [Fig. 8(c)]. The DRB prediction agrees with experiment reasonably well in magnitude but not in radial profile in the steep-gradient edge pedestal region of ELMing H-mode shot 119436 [Fig. 8(a)], but substantially overpredicts the experiment in the same location for the more collisional H-mode phase of shot 118897 [Fig. 8(b)], and substantially underpredicts experiment in the

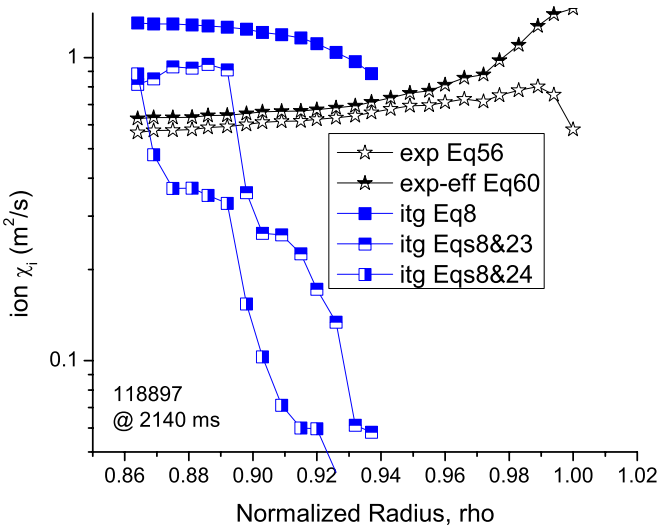

FIG. 11. (Color online) Comparison of ITG prediction of Eq. (8) with experimental ion heat diffusivity, with and without $E\times B$ and magnetic shear suppression for DIII-D ELM-free H-mode shot 118897.

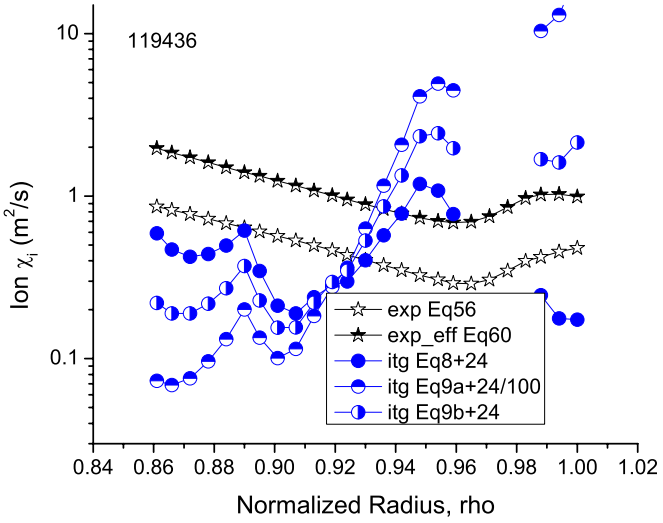

FIG. 13. (Color online) Comparison of ITG predictions of Eqs. (8), (9a), and (9b), all with $E\times B$ and magnetic shear suppression, with the experimental heat diffusivities of Eqs. (56) and (60) for DIII-D ELMing H-mode shot 119436.

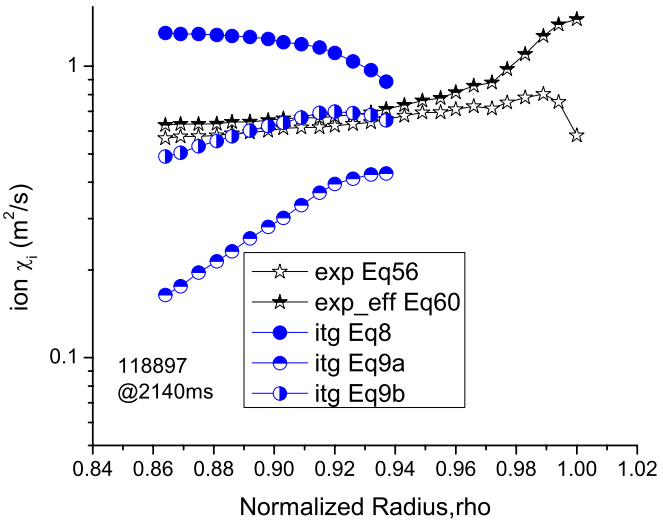

FIG. 14. (Color online) Comparison of ITG predictions of Eqs. (8), (9a), and (9b), all *without* $E\times B$ and magnetic shear suppression, with the experimental heat diffusivities of Eqs. (56) and (60) for DIII-D ELM-free H-mode shot 118897.

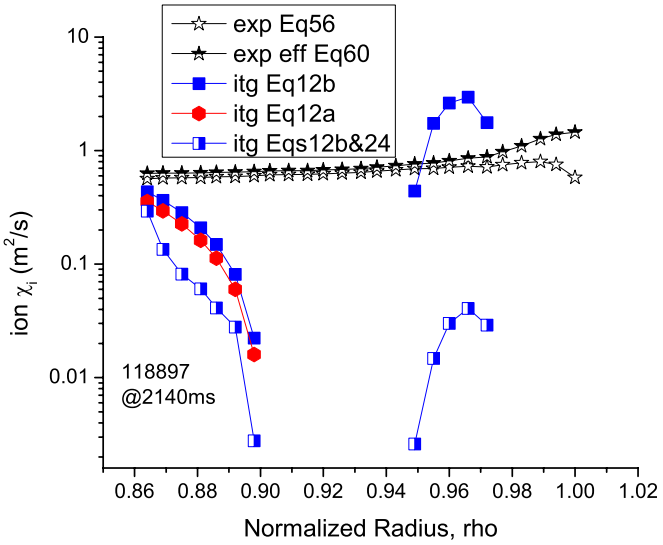

FIG. 16. (Color online) Comparison of ITG prediction of Eqs. (12a) and (12b), with and without $E\times B$ and magnetic shear suppression with experimental ion heat diffusivity for DIII-D ELM-free H-mode shot 118897.

L-mode phase of shot 118897 [Fig. 8(c)]. Clearly, the ETG, paleoclassical, and TEM mechanisms should be further investigated for electron transport in the plasma edge.

VI. SUMMARY AND CONCLUSIONS

The predictions of a number of models for the ion and electron heat diffusivity found in the literature and used today in transport codes have been compared with experimentally inferred values of the heat diffusivity for the edge plasma of two H-mode and one L-mode discharges in DIII-D. Models of ion heat diffusivity based on neoclassical, ion temperature gradient, drift Alfvén, and radiative thermal instability theories, and models of electron heat diffusivity based on paleoclassical, electron temperature gradient, trapped electron, and drift resistive ballooning theories were investigated.

For the L-mode shot, the paleoclassical prediction was in very good agreement with the experimental electron heat diffusivity and the ETG prediction was also reasonably good. None of the theoretical predictions for ion heat diffusivity were in agreement with measurements over the entire edge region, although the radiative thermal instability prediction just inside the separatrix was in reasonable agreement with the experimental ion heat diffusivity.

For the H-mode shots, the best overall agreement with experiment was found with the ITG predictions of ion heat diffusivity. For electron heat diffusivity, the TEM prediction was in reasonable agreement for one shot, and the ETG predictions was in reasonable agreement for the other.

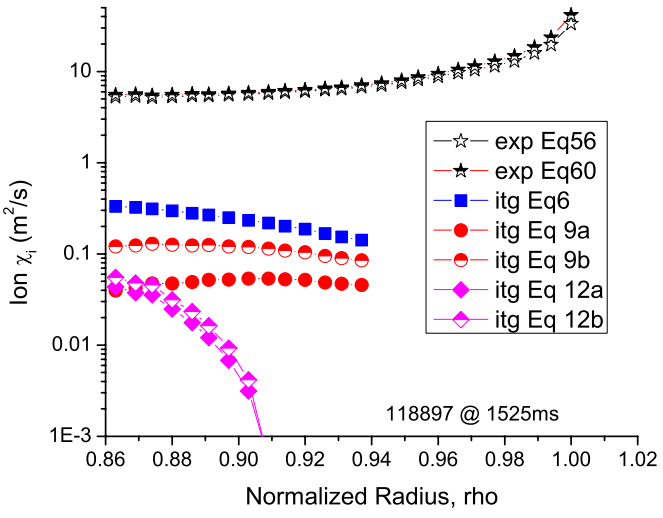

FIG. 15. (Color online) Comparison of ITG predictions of Eqs. (8), (9a), (9b), (12a), and (12b) all *without* $E\times B$ and magnetic shear suppression, with the experimental heat diffusivities of Eqs. (56) and (60) for DIII-D ELM-free L-mode shot 118897.

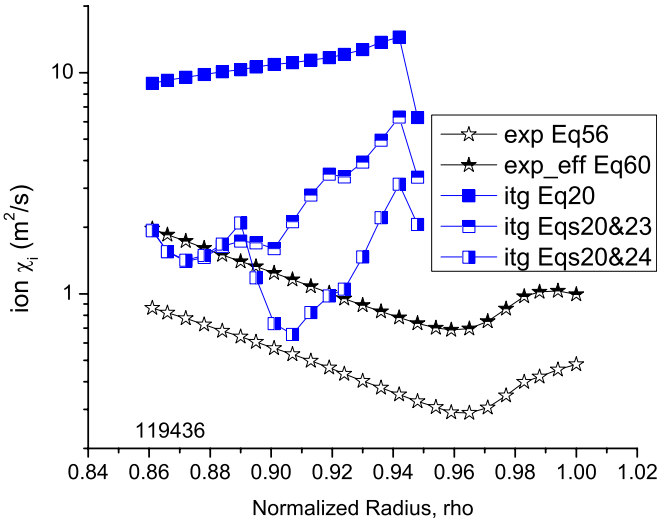

FIG. 17. (Color online) Comparison of ITG prediction of Eq. (20) with experimental ion heat diffusivity, with and without $E\times B$ and magnetic shear suppression for DIII-D ELMing H-mode shot 119436.

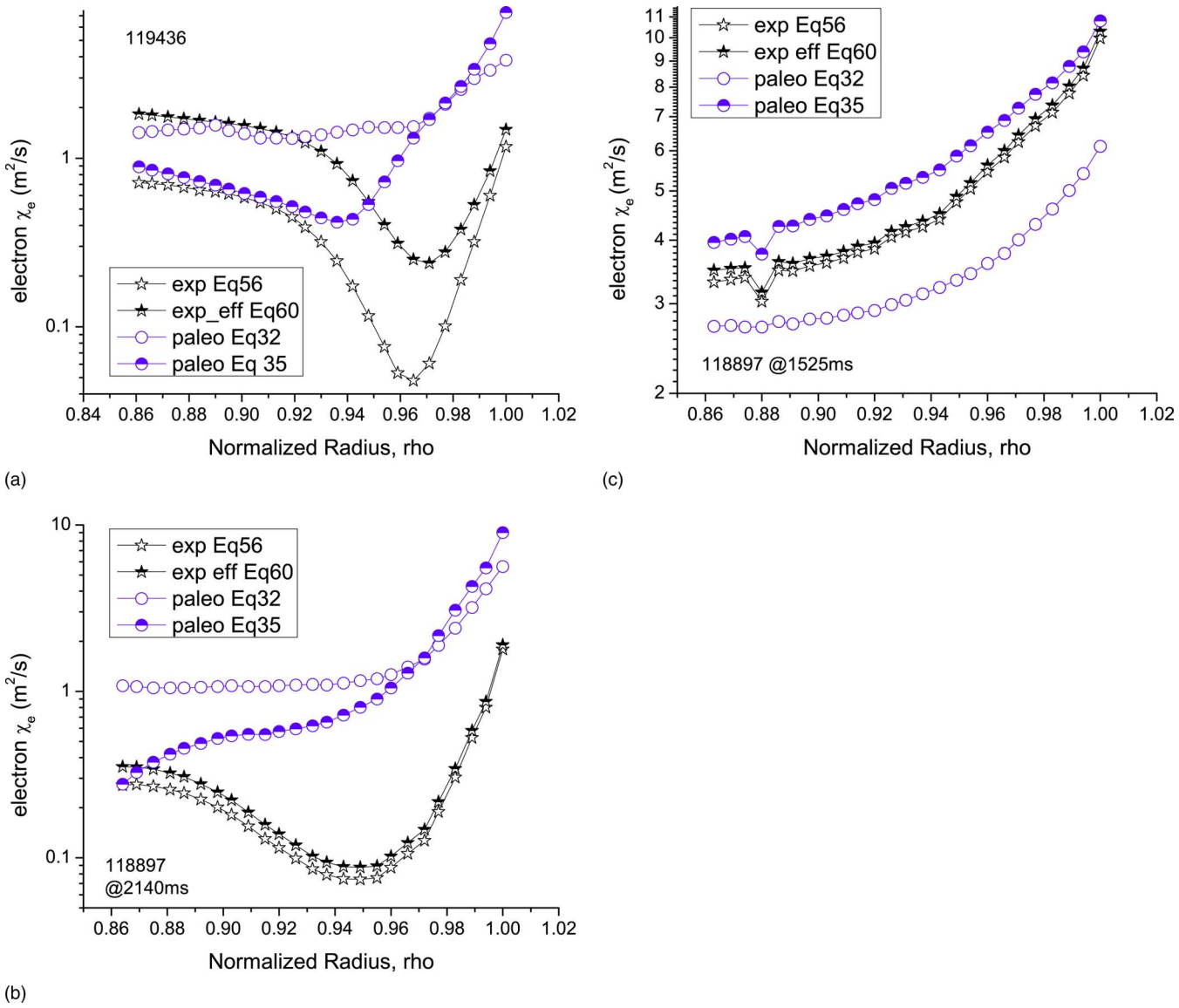

FIG. 18. (Color online) Comparison of paleoclassical and experimental electron heat diffusivities for DIII-D (a) ELMing H-mode shot 119436, (b) ELM-free H-mode shot 118897 at 2140 ms, (c) L-mode shot 118897 at 1525 ms.

ACKNOWLEDGMENTS

The author expresses his appreciation to the other members of the DIII-D team for the measurement and analysis of the data used in this paper, in particular to Rich Groebner for providing the fits used in the calculations, for insightful comments on the paper during its development, and for his contributions to the previous development of methodology for experimental interpretation used in this paper. The author is also grateful to several people for taking their time to discuss various aspects of the theoretical models with him: to Jim Callen for detailed discussions of his paleoclassical model, to Fred Hinton for discussion of the neoclassical model, to Glenn Batemen and Alexie Pankin for discussions of the modeling of various transport mechanisms in the MultiMode model, to Jan Weiland for discussions of his ITG/TEM model, and to Parvez Gudzar for discussion of his DRB model.

This work was supported in part by the U. S. Department of Energy Grant No. DE-FG02-00-ER54538 with the Georgia Tech Research Corporation.

APPENDIX: DETAILED COMPARISONS

Ion heat diffusivities

Neoclassical

The Chang–Hinton neoclassical formula of Eq. (1), with and without the $S_E^{-3/2}$ orbit squeezing correction of Eq. (6), evaluated with experimental data is compared with the inferred experimental thermal diffusivity of Eq. (56) in Fig. 9. Clearly, $\chi_i^{\exp}$ falls near the neoclassical level in the edge region of the H-mode shots, but equally clearly neoclassical theory generally substantially underpredicts the experimental ion heat diffusivity in all shots. The orbit squeezing correction is not very important in these shots.

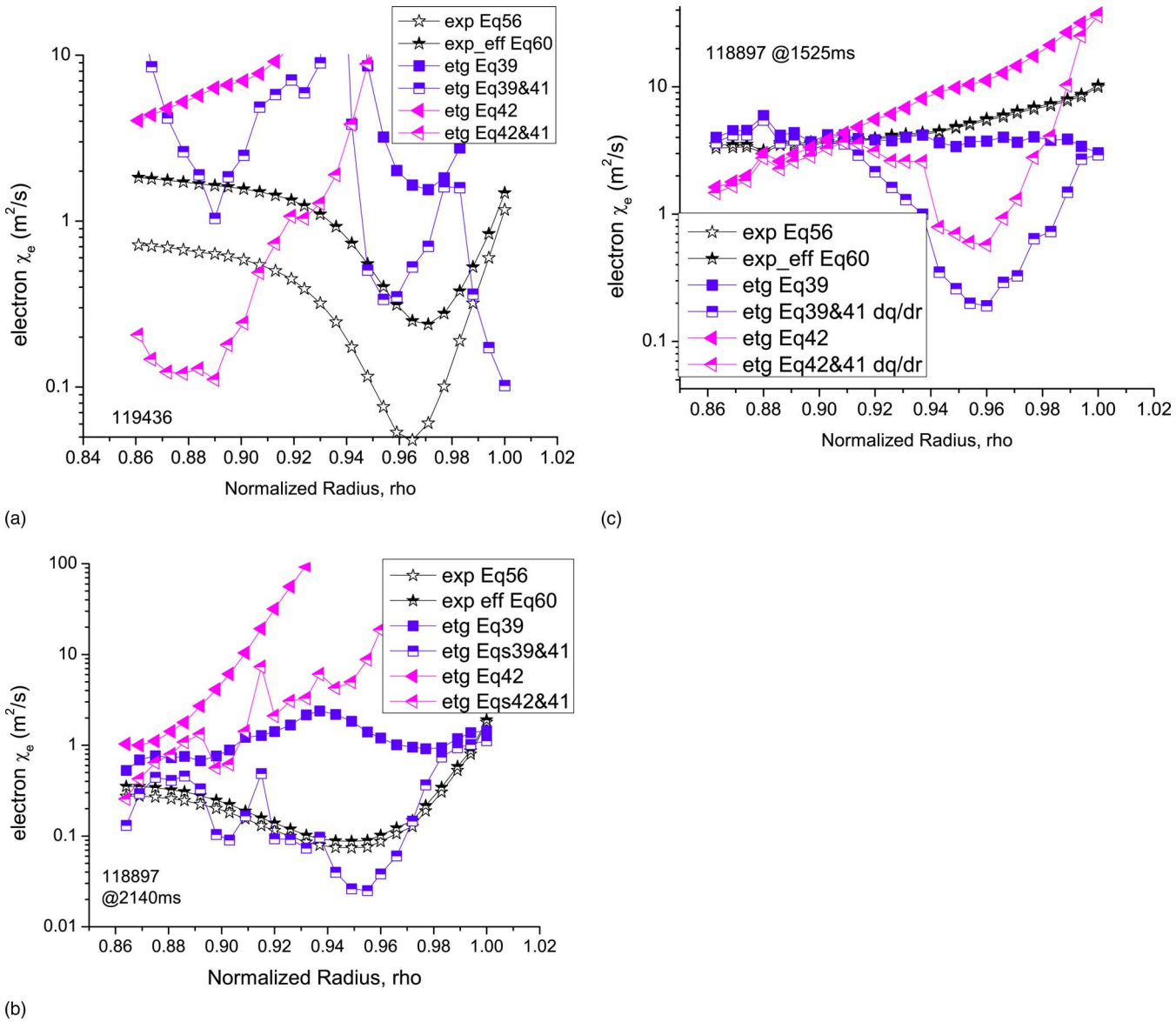

FIG. 19. (Color online) Comparison of ETG heat diffusivity, with and without $E\times B$ and magnetic shear, with experiment in DIII-D (a) ELMing H-mode shot 119436, (b) ELM-free H-mode shot 118897 at 2140 ms, (c) L-mode shot 118897 at 1525 ms.

Ion temperature gradient modes

The criterion $[R/L_{Ti} > (R/L_{Ti})_{\text{crit}}]$ of Eq. (7) plotted in Fig. 3 indicates that ITG transport will exist in the flattop region for all shots and also just inside the separatrix for shot 119436. The prediction of Eq. (8) is plotted for these regions of the edge in Figs. 10–12. The effect of applying the multiplicative $E\times B$ shear suppression factor F_s^{ITG} of Eq. (22), as indicated in Eq. (23), is also shown. (The structure in the shear suppressed results arises from the numerical differentiation of the experimental electric field data of Fig. 5.) The effect of the $E\times B$ shear suppression is quite different for the three cases, corresponding to the differences in the electric field profiles shown in Fig. 5. Also shown is the effect of further applying the multiplicative magnetic shear suppression factor $G(S_m)=S_m^{-1.8}$ as indicated in Eq. (24). This effect is quite different for shots 119436 and 118897, corresponding to the differences in q-profiles shown in Fig. 4.

The experimentally inferred thermal diffusivity of Eq. (56) (calculated using the conductive heat flux) and the effective thermal diffusivity of Eq. (60) (calculated using the total heat flux) are also shown. There is about a factor of 2 difference between the two experimental inferences of heat diffusivity for shot 119436 (for which there is a significant convective heat flux), but almost no difference in shot 118897 (for which the convective heat flux was much smaller).

Predictions of the three simple heuristic ITG formulas—Eqs. (8), (9a), and (9b)—are compared with the experimental heat diffusivities in Figs. 13–15. The factor $C_i=0.014$ found by Horton *et al.*[13] to fit core data for Tore Supra was used in evaluating both Eqs. (9a) and (9b). Note that the prediction of Eq. (9a) has been divided by 100 in Fig. 13 for shot 119436 [i.e., Eq. (9a) with $C_i=0.014$ overpredicts the experimental heat diffusivity by about a factor of 100], but not in

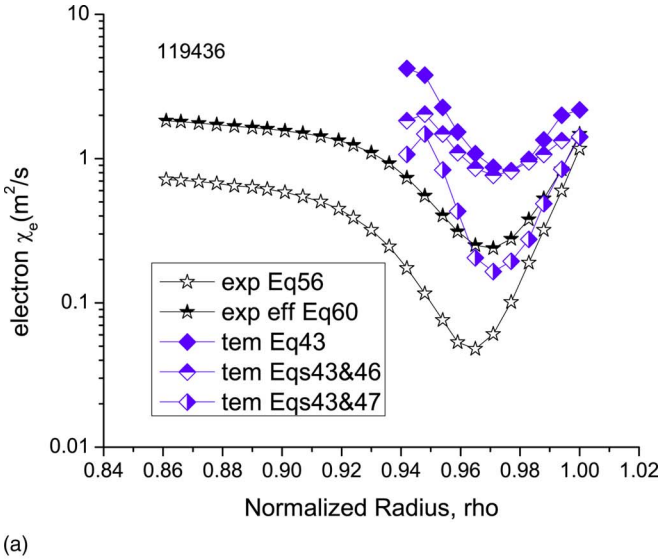

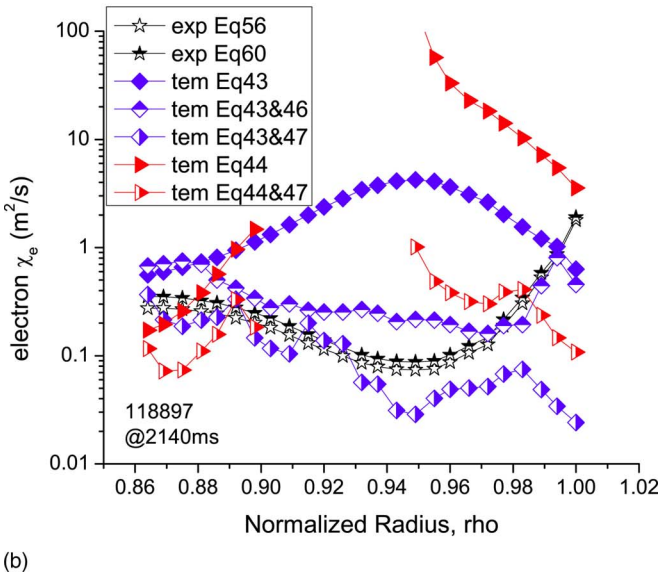

FIG. 20. (Color online) Comparison of TEM electron heat diffusivity, with and without $E\times B$ and magnetic shear, with experiment for DIII-D D (a) ELMing H-mode shot 119436, (b) ELM-free H-mode shot 118897 at 2140 ms.

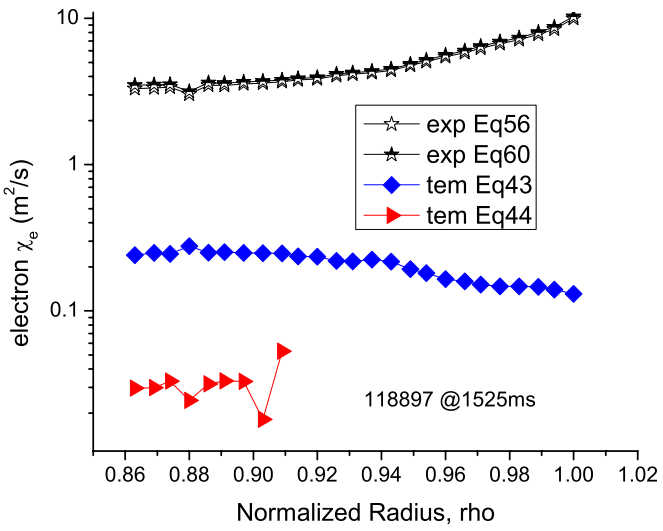

FIG. 21. (Color online) Comparison of TEM electron heat diffusivity, without $E\times B$ and magnetic shear, with experiment for DIII-D ELM-free L-mode shot 118897.

Figs. 14 and 15 for shot 118897. Equation (8) with $E\times B$ suppression and somewhat less magnetic suppression than the $S_m^{-1.8}$ used for shot 119436 would provide a reasonable match with the experimental heat diffusivity, while Eq. (9b) without any shear suppression provides a reasonable match with the experimental heat diffusivity in the flattop region of the H-mode phase of shot 118897.

An attempt to make ITG heat diffusivity predictions using Weiland's model of Eqs. (10), (11), (12a), (12b), and (13)–(19), using $k_\perp = 1/\rho_s$ instead of solving the eigenvalue equation for $k_\perp$ at each mesh point, failed for shot 119436 and met with only limit success for shot 118897. For shot 119436, this evaluation yielded mostly negative values of η_{ITH} which, together with the negative values of η_i in the flattop region mentioned previously, led to mostly complex values of the radical in Eq. (15) for the ITG growth rate. Predictions of Eqs. (12a) and (12b) agreed with predictions of Eq. (9a) in the innermost flattop region for L-mode shot 118897, but all of these were two orders of magnitude smaller than the experimental value, as shown in Fig. 15. Similar results, shown in Fig. 16, were predicted for the H-mode phase of shot 118897, but in this case the agreement with experiment was better at the innermost part of the flattop region.

It was possible to obtain heat diffusivity predictions from the simplified Weiland, or Kalupin *et al.*,[16] model of Eq. (20) in the flattop region of the edge, but not in the steep-gradient edge pedestal region, for shot 119436. These are plotted in Fig. 17, with and without the $E\times B$ and magnetic shear suppression factors. This model comes into a reasonable match with experiment at the innermost part of the flattop region.

Electron heat diffusivities

Paleoclassical

The paleoclassical models for the electron heat diffusivity [Eq. (32)] and "power balance" heat diffusivity [Eq. (35)] are compared with the corresponding inferred experimental values evaluated by using the experimental data in Eq. (56) and Eq. (60), respectively, in Fig. 18. In integrating Eq. (36) to calculate the paleoclassical heat flux profile in the edge, the paleoclassical heat flux at $\rho=0.86$ was set equal to the conductive heat flux at that radius.

The paleoclassical predictions generally agree in magnitude over most of the edge region for the H-mode shots, but do not predict the sharp dip in the experimental heat diffusivities in the steep-gradient edge pedestal region. For the L-mode phase of shot 118897, the paleoclassical prediction agrees extremely well with experiment in both magnitude and profile.

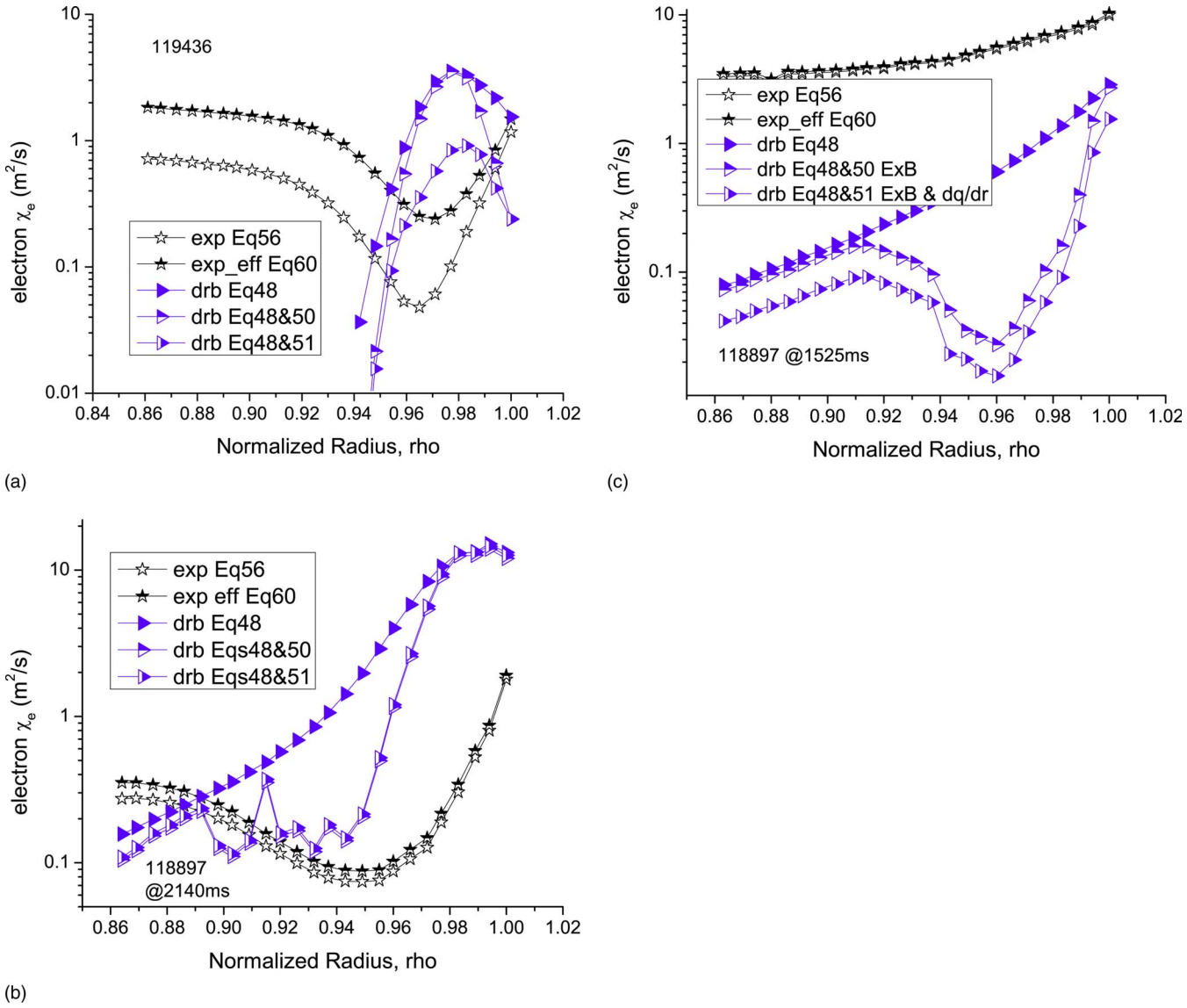

FIG. 22. (Color online) Comparison of DRB heat diffusivity, with and without $E\times B$ and magnetic shear suppression, with experiment in DIII-D D (a) ELMing H-mode shot 119436, (b) ELM-free H-mode shot 118897 at 2140 ms, (c) L-mode shot 118897 at 1525 ms.

Toroidal electron temperature gradient modes

The criterion for the onset of ETG modes, $[R/L_{Te} > (R/L_{Te})_{\text{crit}}]$, was satisfied throughout the edge region in all three shots, indicating that toroidal ETG mode transport would be present. However, the simple expression of Eq. (39) yielded unphysical results for H-mode shot 119436 because of the strange η_e profile shown in Fig. 3, becoming large and negative in the hollow flattop region where $L_n<0$. The more involved Horton *et al.* model[13] of Eq. (42), which takes into account magnetic shear, does not suffer from the same numerical problem but does become several orders of magnitude larger than the experimental value in the steep-gradient pedestal region of shot 119436. Both results are shown in Fig. 19(a), although Eq. (39) results in the $\eta_e<0$ flattop region are questionable.

For both the L- and H-mode phases of shot 118897, the simple ETG expression of Eq. (39) agreed reasonably well with experiment, as shown in Figs. 19(b) and 19(c). The agreement was better in the H-mode phase when the Hamaguchi–Horton shear suppression factor of Eq. (40) was applied (the wiggles in the curve are due to the numerical differentiation of the data in Fig. 5 to evaluate the shear suppression factor), but agreement was better without this factor in the L-mode phase.

Trapped electron modes

For the H-mode shot 119436 with the hollow density profile, the simple Kadomtsev and Pogutse[32] TEM expression of Eq. (43) suffers from the problem mentioned before of $L_n<0$ in the flattop region, but matches the experimental profile quite well in shape and magnitude in the steep-gradient pedestal region where $L_n>0$, as shown in Fig. 20(a). Equation (43) predicts the experimental heat diffusivity reasonably well in magnitude and profile for the H-mode phase of shot 118897 [Fig. 20(b)], when the effects of $E\times B$ and magnetic shear are taken into account, but not for the L-mode phase (Fig. 21). The $E\times B$ shear effect is relatively weak in the steep gradient region in for H-mode shot

119436, but the magnetic shear effect is significant, while both shear suppression effects are significant over the entire edge region for H-mode shot 118897, as found before for the ITG predictions.

The Weiland TEM expression[15] of Eq. (44) suffers from the same problem discussed previously for the ITG mode of a complex value of the growth rate when evaluated with the experimental parameters. When solutions were obtained in H-mode shot 118897 they predicted the experimental order of magnitude [Fig. 20(b)].

Drift resistive ballooning mode

The DRB expression of Eq. (48) suffers also from the $L_n<0$ problem in the flattop for H-mode shot 119436, but the magnitude of the DRB heat diffusivity is small in the flattop region, in any case. In the steep-gradient pedestal region the DRB heat diffusivity is comparable to the experimental value, but the radial profile is different, as shown in Fig. 22(a). Once again, the $E\times B$ shear suppression is small in the steep-gradient region for shot 119436 (note that the $E\times B$ shear suppression factors are different for the DRB and TEM heat diffusivities), but the magnetic shear suppression is significant. For the H-mode phase of shot 118897, the DRB prediction of Eq. (48) agrees in magnitude with the experimental heat diffusivity in the flattop but overpredicts it in the steep-gradient region [Fig. 22(b)], while in the L-mode phase the DRB prediction is well below the experimental value over the entire edge region [Fig. 22(c)].

Resonant magnetic perturbation diffusion

A recent comparison[3] of the predictions of Eqs. (54) and (55) with inferred electron thermal transport showed reasonably good agreement for a DIII-D shot in which the I-coil was used to induce a resonant magnetic perturbation in DIII-D.

[1] J. Luxon, Nucl. Fusion **42**, 614 (2002).
[2] W. M. Stacey and R. J. Groebner, Phys. Plasmas **13**, 072510 (2006).
[3] W. M. Stacey and T. E. Evans, Phys. Plasmas **13**, 112506 (2006).
[4] W. M. Stacey and R. J. Groebner, Phys. Plasmas **14**, 012501 (2007).
[5] W. M. Stacey and R. J. Groebner, Phys. Plasmas **14**, 122504 (2007).
[6] J. E. Kinsey, R. E. Waltz, and J. Candy, Phys. Plasmas **14**, 102306 (2007).
[7] C. S. Chang and F. L. Hinton, Phys. Fluids **25**, 1493 (1982).
[8] C. S. Chang and F. L. Hinton, Phys. Fluids **29**, 3314 (1986).
[9] J. A. Wesson, *Tokamaks*, 2nd ed. (Clarendon, Oxford, 1997).
[10] K. C. Shaing and R. D. Hazeltine, Phys. Fluids B **4**, 2547 (1992).
[11] F. Jenko, W. Dorland, and G. W. Hammett, Phys. Plasmas **8**, 4096 (2001).
[12] F. Romanelli, W. M. Tang, and R. B. White, Nucl. Fusion **26**, 1515 (1986).
[13] W. Horton, P. Zhu, G. T. Hoang, T. Aniel, M. Ottaviani, and X. Garbet, Phys. Plasmas **7**, 1494 (2000).
[14] M. Ottaviani, W. Horton, and M. Erba, Plasma Phys. Controlled Fusion **39**, 1461 (1997).
[15] J. Weiland, *Collective Modes in Inhomogeneous Plasmas* (IOP, Bristol, 2000).
[16] D. Kalupin, M. Z. Tokar, B. Unterberg, X. Loozen, and D. Pilipenko, Nucl. Fusion **45**, 468 (2005).
[17] T. S. Halm and K. H. Burrell, Phys. Plasmas **2**, 1648 (1995).
[18] P. W. Terry, Rev. Mod. Phys. **72**, 109 (2000).
[19] A. Y. Pankin, I. Toitsekhovitch, G. Bateman, A. Denestrovski, G. Janeschitz, M. Murakami, T. Osborne, A. H. Kritz, T. Onjun, G. W. Pacher, and H. D. Pacher, Plasma Phys. Controlled Fusion **47**, 483 (2005).
[20] O. V. Zolotukhin, Y. Igitkhanov, G. Pacher, G. Janeschitz, and H. Pacher, *28th EPS Conference on Controlled Fusion and Plasma Physics*, Funchal, Portugal, 2001 (IAEA, Vienna, 2002), p. 677.
[21] G. Janeschitz, G. W. Pacher, O. Zolotukhim, G. Pereverzev, H. D. Pacher, Y. Igitkhanov, G. Strohmeyer, and M. Sugihara, Plasma Phys. Controlled Fusion **44**, A459 (2002).
[22] G. Pacher, H. Pacher, G. Janeschitz, A. Kukushkin, and G. Pereverzev, Plasma Phys. Controlled Fusion **46**, A257 (2004).
[23] M. Sugihara, Yu. Igitkhanov, G. Janeschitz, A. Hubbard, Y. Kamada, J. Lingertat, T. H. Osborne, and W. Suttrop, Nucl. Fusion **40**, 1743 (2000).
[24] T. S. Hahm and P. H. Diamond, Phys. Fluids **30**, 133 (1987).
[25] B. N. Rogers, J. F. Drake, and A. Zeiler, Phys. Rev. Lett. **81**, 4396 (1998).
[26] W. Kerner, Contrib. Plasma Phys. **38**, 118 (1998).
[27] W. M. Stacey, Phys. Plasmas **6**, 2452 (1999).
[28] J. D. Callen, Nucl. Fusion **45**, 1120 (2005).
[29] J. D. Callen, University of Wisconsin, personal communication (2007).
[30] S. Hamaguchi and W. Horton, Phys. Fluids B **4**, 319 (1992).
[31] G. Bateman, A. H. Kritz, A. Y. Pankin, T. Onjun, J. E. McElhenny, and C. McDonald, Plasma Phys. Controlled Fusion **48**, A93 (2006).
[32] B. Kadomtsev and O. Pogutse, Nucl. Fusion **11**, 67 (1971).
[33] D. R. McCarthy, P. N. Gudzar, J. F. Drake, T. M. Antonsen, and A. B. Hassam, Phys. Fluids B **4**, 1846 (1992).
[34] P. N. Gudzar, J. F. Drake, D. R. McCarthy, A. B. Hassam, and C. S. Liu, Phys. Fluids B **5**, 3712 (1993).
[35] G. Bateman, A. H. Kritz, J. E. Kinsey, A. J. Redd, and J. Weiland, Phys. Plasmas **5**, 1793 (1998).
[36] P. Gudzar, R. G. Kleva, A. Das, and P. K. Kaw, Phys. Rev. Lett. **87**, 015001 (2001).
[37] T. E. Evans, R. A. Moyer, and P. Monat, Phys. Plasmas **9**, 4957 (2002).
[38] L. W. Yan and T. E. Evans, J. Nucl. Mater. **363–365**, 723 (2007).
[39] W. M. Stacey, E. W. Thomas, and T. M. Evans, Phys. Plasmas **2**, 3740 (1995); **4**, 678 (1997).
[40] R. Hulse, Nucl. Technol./Fusion **3**, 259 (1983).
[41] W. M. Stacey, Phys. Plasmas **5**, 1015 (1998); **8**, 3673 (2001); Nucl. Fusion **40**, 678 (2000).